Seasonal patterns of atmospheric mercury in tropical South America as inferred by a TGM continuous record at the Chacaltaya Station (5240 m) in Bolivia

Authors:

Alkuin Maximilian Koenig[1], Olivier Magand[1], Paolo Laj[1], Marcos Andrade[2,7], Isabel Moreno[2], Fernando Velarde[2], Grover Salvatierra[2], René Gutierrez[2], Luis Blacutt[2], Diego Aliaga[3], Thomas Reichler[4], Karine Sellegri[5], Olivier Laurent[6], Michel Ramonet[6], and Aurélien Dommergue[1]

Affiliations

[1] Institut des Géosciences de l'Environnement, Université Grenoble Alpes, CNRS, IRD, Grenoble INP, Grenoble, France

[2] Laboratorio de Física de la Atmósfera, Instituto de Investigaciones Físicas, Universidad Mayor de San Andrés, La Paz, Bolivia

[3] Institute for Atmospheric and Earth System Research/Physics, Faculty of Science, University of Helsinki, Helsinki, 00014, Finland

[4] Department of Atmospheric Sciences, University of Utah, Salt Lake City, 84112, USA

[5] Université Clermont Auvergne, CNRS, Laboratoire de Météorologie Physique, UMR 6016, Clermont-Ferrand, France

[6] Laboratoire des Sciences du Climat et de l'Environnement, LSCE-IPSL (CEA-CNRS-UVSQ), Université Paris-Saclay, 91191 Gif-sur-Yvette, France

[7] Department of Atmospheric and Oceanic Sciences, University of Maryland, College Park, MD, USA

Correspondence to: alkuin-maximilian.koenig@univ-grenoble-alpes.fr

Abstract

High-quality data of atmospheric mercury (Hg) is rare for South America, especially for its tropical part. In consequence, mercury dynamics are still highly uncertain in this region, a significant deficiency, as South America appears to play a major role in the global budget of this toxic pollutant. To address this issue, we performed nearly two years (July 2014 - February 2016) of continuous high resolution total gaseous mercury (TGM) measurements at the Chacaltaya (CHC) mountain site in the Bolivian Andes, which is subject to a diverse mix of air masses coming predominantly from the Altiplano and the Amazon rainforest. For the first eleven months of measurements, we obtained a mean TGM concentration of $0.89 \pm 0.01\ ng\ m^{-3}$, in good agreement with the sparse amount of data available from the continent. For the remaining nine months, we obtained a significantly higher TGM concentration of $1.34 \pm 0.01\ ng\ m^{-3}$, a difference which we tentatively attribute to the strong "El Niño" event of 2015 - 2016. Based on HYSPLIT back-trajectories and clustering techniques, we show that lower mean TGM concentrations were linked to either westerly Altiplanic air masses or those originating from the lowlands to the south-east of CHC. Elevated TGM concentrations were related to northerly air masses of Amazonian or southerly air masses of Altiplanic origin, the former possibly linked to artisanal and small scale gold mining (ASGM), while the latter might be explained by volcanic activity. We observed a marked seasonal pattern, with low TGM concentrations in the dry season (austral winter), rising concentrations during biomass burning (BB) season, and highest concentrations at the beginning of the wet season (austral summer). With the help of simultaneously sampled equivalent black carbon (eBC) and carbon monoxide (CO) data, we use the clearly BB influenced signal during BB season (August to October) to derive a mean TGM/CO emission ratio of $(2.3 \pm 0.6) \cdot 10^{-7} ppbv_{TGM}\ ppbv_{CO}{}^{-1}$, which could be used to constrain South American BB emissions. Through the link with in-situ measured CO_2 and remotely sensed solar-induced fluorescence (SIF) as proxies for vegetation activity, we detect signs of a vegetation sink effect in Amazonian air masses and derive a "best guess" TGM/CO_2 *uptake ratio* of $-0.058 \pm 0.017\ (ng\ m^{-3})_{TGM}\ ppm_{CO2}{}^{-1}$. Finally, significantly higher Hg concentrations in western Altiplanic air masses during the wet season as compared to the dry season point towards the modulation of atmospheric Hg by the Eastern Pacific Ocean.

1. Introduction

Mercury (Hg) is a global contaminant that accumulates in the marine food chain and thus threatens wildlife and populations relying on halieutic resources. In 2017, the Minamata convention was implemented to decrease human exposure to this toxic compound by targeting particularly anthropogenic Hg emissions. It is estimated that humanity has increased atmospheric Hg concentrations by a factor of ~2.6 since the pre-industrial era and that legacy Hg is being recycled in the environment (Beal et al., 2014; Lamborg et al., 2014, Obrist et al., 2018). As reported in the 2018 Global Mercury Assessment, anthropogenic sources of Hg comprise mainly artisanal and small scale gold mining (ASGM, accounting for about 38% of the total emissions in 2015), stationary fossil fuel and biomass combustion (24%), metal and cement production (combined 26%) and garbage incineration (7%).

Hg exists in the atmosphere mostly as gaseous elemental mercury (GEM) and oxidized gaseous species (GOM), with the sum of both often being referred to as total gaseous mercury (TGM). Over the last 15 years, TGM and GEM are being monitored worldwide by regional, national, and continental initiatives alongside networks such

as GMOS (Global Mercury Observation System), AMNet (Atmospheric Mercury Network), MDN (Mercury Deposition Network), and APMMN (Asia-Pacific Mercury Monitoring Network). These measurements provide a tool to rapidly follow changes and patterns in sources and understand regional processes.

Nevertheless, the global coverage of these measurements is far from evenly distributed. While many monitoring sites exist in the Northern Hemisphere, especially China, North America, and Europe, surface observations are sparse in the tropics and the Southern Hemisphere (Howard et al., 2017; Obrist et al., 2018; Sprovieri et al., 2016; Global Mercury Assessment, 2018). In South America, only a few studies have observations to explore the seasonal and multiannual trends of atmospheric Hg. Guédron et al. (2017) give a short record of TGM measured at the Titicaca lake in the Bolivian/Peruvian Andes, while Diéguez~~Dieguez~~ et al. (2019) provided a multi-annual, but not continuous record of atmospheric Hg species in Patagonia, Argentina. GEM averages for Manaus in the Amazon rainforest of Brazil were also reported by Sprovieri et al. (2016). Müller et al. (2012) measured TGM during 2007 in Nieuw Nickerie, Suriname, in the Northern part of South America. ~~,~~ Lastly, some data on South American upper tropospheric TGM concentrations is provided by CARIBIC flights (https://www.caribic-atmospheric.com/) for the routes with~~Frankfurt to~~ São Paulo, ~~and São Paulo to~~ Santiago de Chile, Bogota, or Caracas as destination (Slemr et al., 2009, 2016).

This lack of data is problematic, as South America plays an important role in the global mercury budget. In 2015, about 18% of global mercury emissions occurred on this continent, where widespread ASGM is thought to be the major contributor (Global Mercury Assessment, 2018). Worldwide, around 53% of the estimated ASGM releases are attributed to South America, but the uncertainties regarding their exact quantity and spatial distribution are large (Global Mercury Assessment, 2018). Furthermore, the role of the world's largest tropical rainforest, the Amazon, has not yet been clearly determined, even though this large pool of vegetation may importantly modulate the seasonal cycle of mercury (Jiskra et al., 2018) through mechanisms such as the substantial storage of Hg in plant litter (Jiskra et al., 2015) and a posteriori re-emission in large-scale biomass burning (BB) events (Fraser et al., 2018; Webster et al., 2016). The highly vegetated Amazon region is very sensitive to external changes (Phillips et al., 2008) and undergoes a constant shift in behavior. On the one hand, there are natural changes, like the El-Niño-Southern Oscillation (ENSO), which strongly affects moisture transport and precipitation over South America and the Amazon (Ambrizzi et al., 2004; Erfanian et al., 2017). On the other hand, there are anthropogenic perturbations, like land-use and climate changes. Both types of variations may greatly and durably alter the equilibrium of the Amazon rainforest ecosystem, with important regional and global consequences (Fostier et al., 2015; Obrist et al., 2018; Phillips et al., 2008).

The goal of this study is to partly overcome the TGM data gap over South America by providing new high-quality Hg measurements from the Global Atmosphere Watch (GAW) station Chacaltaya (CHC), a distinctive site due to its location in the tropical part of the Andes, at 5240 m above sea level. Between July 2014 and February 2016, we continuously measured TGM at the CHC station, which allowed us to sample air masses of both Altiplanic and Amazonian origin. Through this unique data set, we explore the seasonal pattern of TGM in the region and discuss possible sources and sinks for atmospheric mercury in the South American tropics.

2. Methodology

2.1 Site description

Measurements were conducted at the CHC GAW regional station (WMO region III – South America, 16°21.0140 S, 68°07.8860 W), at an altitude of 5240 m a.s.l, about 140 m below the summit of mount Chacaltaya on the eastern edge of the "Cordillera Real" (Fig. 1, Andrade et al., 2015), with a horizon open to the South and West. Measurements of general meteorology, CO_2, CO, CH_4, O_3 and aerosol properties are performed continuously. The area surrounding the station is stony, sparsely vegetated and with intermittent snow cover (especially in the wet season). The site is located at about 17 km north of the urban agglomeration La Paz/El Alto with more than 1.8 million inhabitants and in spite of its high elevation, it is frequently influenced by air masses arriving from the boundary layer of the Altiplano. Thermally-induced circulation is regularly observed between about 9:00 and 12:00 local time through an increase in equivalent black carbon (eBC), carbon monoxide (CO), and particulate matter (Andrade et al., 2015; Rose et al., 2017, Wiedensohler et al., 2018). However, cleaner conditions can be observed during nighttime, when the site lies in quasi-free tropospheric conditions (Andrade et al., 2015; Chauvigné et al., 2019; Rose et al., 2017).

CHC is relatively close (~300 km distance) to the "Madre de Dios" watershed, a known hot spot for ASGM (Beal et al., 2013; Diringer et al., 2015, 2019). Apart from this prominent region, many other sites of ASGM exist in the Bolivian, Peruvian and Brazilian lowlands, but little exact information is available due to their intrinsically poorly documented and unregulated nature.

Finally, starting in northern Chile, extending all along the Bolivia-Chile border and reaching into Peru, we find the central volcanic zone (CVZ), where several volcanoes have been reported to be actively degassing, both to the south (Tamburello et al., 2014; Tassi et al., 2011) and to the west of CHC (Moussallam et al., 2017). This entire volcanic arc showed above long-term average SO_2 emissions in 2015 (Carn et al., 2017).

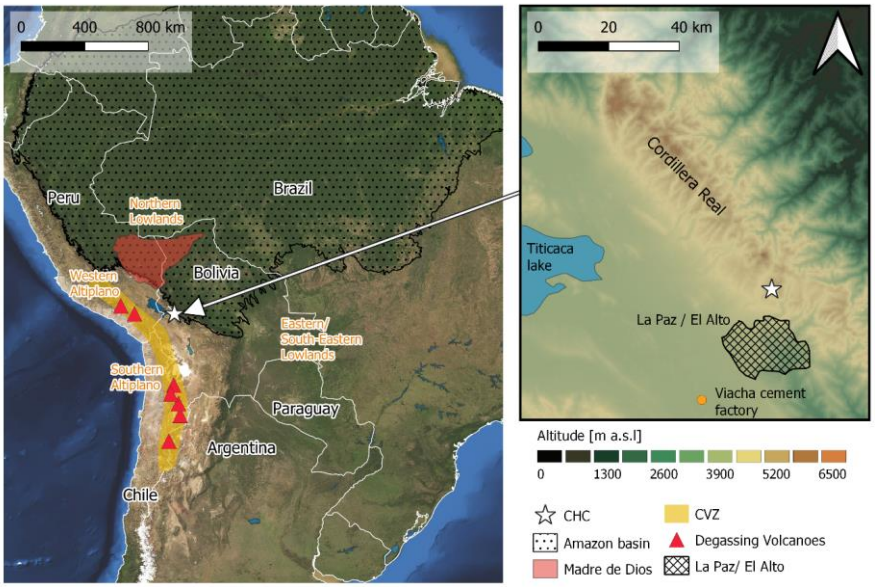

Fig. 1 : Left: True color satellite image (from ESRI) of the location of CHC station (star) on the continent, with the "Madre de Dios" watershed shaded in red, the Central Volcanic Zone (CVZ) in yellow and the extent of the Amazon~~amazon~~ basin as dotted surface (used Amazon shapefile: http://worldmap.harvard.edu/data/geonode:amapoly_ivb). Air mass origins as used in this work in orange. Selected degassing volcanoes in the CVZ are shown as red triangles, from north to south: Sabancaya, Ubinas, Ollague, San Pedro, Putana, Lascar, Lastarria. Right: Zoomed in map with color coded elevation. The hatched area represents the metropolitan area of La Paz /El Alto, the orange dot shows the cement factory "Cemento Soboce" in the town of Viacha.

Field Code Changed

2.2 Data

2.2.1 TGM measurements

Atmospheric total gaseous mercury (TGM) has been measured at CHC GAW station from July 2014 to February 2016, using a 2537A Tekran analyzer model (Tekran Inc., Toronto, Canada). Concentrations are expressed in nanograms per cubic meter at STP conditions (273.15 K, 1013.25 hPa). The instrument is based on mercury enrichment on a gold cartridge, followed by thermal desorption and detection by cold vapour atomic fluorescence spectroscopy (CVAFS) at 253.7 nm (Fitzgerald and Gill, 1979; Bloom and Fitzgerald, 1988). Switching between two cartridges allows for alternating sampling and desorption and thus results in full temporal coverage of the atmospheric mercury measurement. During the 20-month measurement period, the instrument was automatically calibrated every 4 days on average, using an internal mercury permeation source. The latter was annually checked against manual injections of saturated mercury vapor taken from a temperature-controlled vessel, using a Tekran 2505 mercury vapor calibration unit and a Hamilton digital syringe, and following a strict procedure adapted from

Dumarey et al (1985). Atmospheric air, sampled through an unheated and UV protected PTFE sampling line and inlet installed outside at 6 m a.g.l., was previously filtered by two 4.5 µm and 0.5 µm 47 mm filters before entering the Tekran, in order to prevent any particulate matter to be introduced into the detection system. The instrument worked with a flow rate of 0.7 L/mn at STP conditions, which was permanently checked by a *Tylan* calibrated and certified internal mass flow meter. In addition to that, every three months the flow rate was controlled manually with an external volumetric flow meter.

The range of TGM concentrations measured during the entire period (43 732 data points) was 0.42 to 4.55 ng m^{-3}, with the detection limit of the instrument being below 0.1 ng m^{-3}. Given a time resolution of 15 min and a sampling flow rate of 0.70 l (STP) min^{-1}, this corresponds to mercury mass loads on the gold cartridges between ~ 5 pg and ~ 48 pg per cycle (average collection of 11.3 pg), and 54% and 81% of the mercury loading per cycle being above 10 and 8 pg, respectively.

Since the instrument is limited by local low pressure (540 mbar) at the high altitude CHC station and considering the range of detected concentrations, the default peak integration parameters were quickly optimized to avoid any low bias of measurements due to the internal Tekran integration procedure (Ambrose, 2017; Slemr et al., 2016~~2016a~~; Swartzendruber et al., 2009). Non-linear integration responses for mercury mass loading below 10 pg per cycle have been observed with non-adjusted parameters that control the detection of the end of the peak (NBase and VBase). The latter were improved as stated by Swartzendruber et al. (2009), ensuring high-quality detection conditions in this very atypical atmospheric station, the highest in the world, where the Tekran analyzer, as well as all measurement systems, run in very stringent environmental conditions.

To ensure the comparability of the mercury measurements regardless of the study site, the Tekran instrument has been operated according to the GMOS (Global Mercury Observation System) standard operating procedures (SOP, Munthe et al., 2011), in accordance with best practices on measurements adopted in well-established regional mercury monitoring networks (CAMNet, AMNet). Raw dataset, routine, and exceptional maintenance/monitoring files were compiled and processed by software developed at IGE and specifically designed to quality assure and quality control atmospheric mercury datasets in order to produce clean TGM time series. In this automated process, the raw dataset is compared against potential flags corresponding to more than 40 criteria that specifically refer to all operation phases related to the calculation of mercury concentrations and calibration (D'Amore et al., 2015). Each raw observation is individually flagged depending on the result of each corresponding criterion and returns, as a temporary output, a flagged dataset (valid, warning, and invalid). Inclusion of all field notes, implying corrections and invalidations of data regrouped in the flagged dataset step, as well as a clarification step by the site manager according to his knowledge allows for the production of a complete QAed/QCed dataset according to the initial temporal acquisition resolution.

2.2.2 CO measurements

Atmospheric CO mixing ratio was measured at CHC with a 1-min integration time using a non-dispersion cross-modulation infrared analyzer (model APMA-370, HORIBA Inc.). The sample air was pulled from the outside at about 0.8 L min^{-1} through a 2-m Teflon line. The lower detectable limit is 50 [nmol mol^{-1}] and the instrument was set up to measure in the scale of 0-5 [µmol mol^{-1}].

2.2.3 eBC measurements

At CHC, the atmospheric black carbon mass concentration is continuously measured by a Multi-Angle Absorption Photometer (MAAP) (model 5012, Thermo Inc.). The MAAP is a filter-based instrument that utilizes a combination of light reflection and transmission measurements at 637 nm (Müller et al., 2011) together with a radiative transfer model to yield the black carbon concentration using a constant mass absorption cross section~~MAC~~ of 6.6 m^2 g^{-1} (Petzold & Schönlinner, 2004). As black carbon by definition cannot be unambiguously measured with filter-based instruments, it's customary to call the measured light absorbing constituent as equivalent black carbon (eBC) (Bond & Bergstrom, 2006). The sample air is conducted to the instrument through 1.5 meters of a conductive tube from the main inlet that is equipped with an automatic heating system and a whole-air sampling head. Data based on 1-min were recorded, and their hourly averages were used for the analysis given a detection limit of 0.005 µg m^{-3}.

2.2.4 CO_2 measurements

Atmospheric CO_2 concentrations have been measured with a cavity ring-down spectrometer (CRDS) analyzer from Picarro (model: G2301). This analyzer measures every 2-3 seconds the concentration of CO_2, CH_4 and H_2O. The analyzer was calibrated upon a suite of four calibrated compressed air cylinders provided by LSCE central laboratory (calibrated against the WMO scale) every two to four weeks, and quality control of the data was ensured by regular analysis of two target gases (with known and calibrated concentrations); one short term target gas analyzed for 30 min at least twice a day and one long term target gas analyzed for 30 min during the calibration procedure. Those regular measurements indicate a repeatability of 0.04 ppm. Ambient air is pumped from the roof platform through a dekabon tubing. The Picarro analyzer enables the measurement of atmospheric moisture content, which is used to correct the measured GHG concentrations.

2.2.5 Hourly data averaging

We generally worked with hourly averages to allow for easy synchronization of measurements from different instruments. Hourly averages were based on the arithmetic mean of all data taken within an hour (starting at 0 and ending at 59 minutes). In the case of TGM, if more than 50% of the singular data points within an hour were invalid (missing data or flagged as bad data), a no-data value was assigned to the respective hourly average and it was excluded from further analysis. In the case of CO_2, were measurements were obtained every few seconds, the hourly averages were based on previously computed minute averages.

2.2.6 Uncertainties and confidence intervals

All uncertainties of mean concentrations are expressed as two times the standard error of the mean (SEM), giving approximately a 95% confidence interval when comparing subsets of data measured at CHC, under the assumption of constant systematic uncertainty. When comparing CHC data to other stations, we suggest using this value only if it is higher than the average estimated systematic uncertainty for the respective instrument. In the case of the Tekran analyzer, this is about 10% of the measured value (Slemr et al., 2015).

The approximately 95% confidence interval for medians in box plots, shown as a notch, is based on the equation $median_{upper/lower} = median \pm 1.58 \cdot \frac{IQR}{\sqrt{n}}$, where IQR is the inter-quartile-range and n is the number

of data points (McGill et al., 1978). As in the case of the SEM, we advise using the systematic uncertainty of the respective instrument when comparing to other measurement sites.

Robust linear models (iteratively reweighted least squares) and their confidence intervals at a level of 95% were computed using the MASS package for R (Venables and Ripley, 2002). Confidence intervals are displayed in square brackets.

2.2.7 Solar induced fluorescence (SIF/ SIFTER)

As a remotely sensed proxy for vegetation activity, we examined satellite data on solar induced fluorescence (SIF). More concretely, the SIFTER v2 product described in Koren et al. (2018), provided under the DOI https://doi.org/10.18160/ECK0-1Y4C , and based on the TEMIS SIFTER v2 product, which uses GOME-2A data (Kooreman et al., 2020). SIF has been shown previously to be a good proxy for photosynthetic activity and gross primary production (GPP), (Frankenberg et al., 2011; Koren et al., 2018; Qiu et al., 2020; Sanders et al., 2016; Zhang et al., 2014). Particularly, satellite obtained SIF is thought to be a more direct measure of plant chemistry than retrieval products based on spectral reflectance, such as the NDVI and EVI (Luus et al., 2017; Zhang et al., 2014). Following the same procedure as described in Koren et al. (2018), we accounted for GOME-2A sensor degradation by linear detrending and obtained an identical time series for the average monthly SIFTER over the entire (legal) Amazon rainforest, which we later used as a proxy for amazon GPP to establish a connection between the variation in mercury levels and vegetation activity (The amazon mask can be found here: doi:10.18160/P1HW-0PJ6).

Field Code Changed

Formatted: Font: Arial, 11 pt

2.2.8 The Oceanic Niño Index (ONI)

To assess the possible influence of "El Nino Southern Oscillation" (ENSO), we deployed the ONI index, which is based on the sea surface temperature (SST) anomaly in the Nino 3-4 region (5N - 5S, 170W - 120W). It is the main index used by NOAA to evaluate the strength of ENSO events and can be obtained at: https://origin.cpc.ncep.noaa.gov/products/analysis_monitoring/ensostuff/ONI_v5.php

2.3 Definition of seasonal periods

Air masses arriving at CHC have been reported to show a strong seasonal dependency, both in their origin and the magnitude of biomass burning (BB) influence (Chauvigné et al., 2019; Rose et al., 2015). As in previous studies about CHC station, we grouped the year into three main seasonal periods ("seasons"), which we define as follows:

- The not strongly BB impacted part of the dry season (Here short: Dry season) from May to the end of July, climatologically characterized by predominant highland (Altiplanic) influences and low moisture content. Part of austral winter.
- The BB season from August to the end of October. During this time of the year, forest fires tend to be most common in the region (Graciela et al., 2011; Morgan et al., 2019, also compare to Fig. A1 in Appendix A) and important BB influences are registered at CHC. At the beginning climatologically comparable to the dry season, but with quickly increasing lowland influences along its course.

- The wet season from December to the end of March. During this time of the year, lowland (Amazonian) influences and moisture content are highest and BB is mostly insignificant. This season coincides with austral summer.

We furthermore considered the remaining months of the year, April and November, to be "transition months" between the mentioned seasons and did not include them in the seasonal analysis.

2.4 Air mass origin at the regional scale

To identify common pathways of air mass origin and transport, we used the same set of HYSPLIT back trajectories as already described in Chauvigné et al. (2019). Briefly, for every hour of the day, a 96-hour runtime HYSPLIT back trajectory (Stein et al., 2015) was computed for each of nine arrival points located at 500 meter above ground, and within a 2 km x 2 km square grid around the station. The input meteorological fields for the HYSPLIT simulations were obtained from ERA interim and dynamically downscaled using the Weather Research and Forecasting (WRF) model to increasing nested spatial resolutions of 27 km, 9.5 km, 3.17 km, and finally 1.06 km to account for the complex topography of the site.

Additionally, we worked with the air mass classification results introduced in the same work, obtained by applying k-means clustering to the temporal signatures (number of back-trajectory piercings per month of the year) of geographical cells on a log-polar grid (Chauvigné et al., 2019). Their method, applied to HYSPLIT back trajectories between January 2011 and September 2016, yielded six prevalent clusters of air mass origin. They are shown in Fig. 2 and can be shortly described as follows:

Formatted: Subscript

- Cluster C1: Northern lowlands. Air masses of Amazonian origin, which take a southward turn after hitting the Andes (Graciela et al., 2011). Includes the very ASGM active "Madre de Dios" watershed.
- Cluster C2: Eastern/South-Eastern lowlands. Includes scrublands like the dry Chaco region between Bolivia and Paraguay, but also the Pantanal wetland at the eastern frontier to Brazil.
- Cluster C3: Northern Chile/Southern Altiplano. Includes actively degassing volcanoes of the CVZ (Tamburello et al., 2014; Tassi et al., 2011) and the La Paz valley.
- Cluster C4: Eastern edge of the Altiplano. Air masses passing to the east of the Titicaca lake.
- Cluster C5: Western altiplano. Includes the Titicaca lake, Peruvian highland, and the Pacific Ocean, also passes over parts of the CVZ (Moussallam et al., 2017).
- Cluster C6: Cloud forest at the North-eastern edge of the Cordillera Real.

By following Eq. (1), Chauvigné et al. (2019) computed the relative influence of the six clusters, expressed as a percentage, for each hour of the day.

$$P_i(t) = \frac{\sum_{k \in C_i} n_k(t) w_k}{\sum_{k \in C_n} n_k(t) w_k} \cdot 100\% \quad (1)$$

Where $P_i(t)$ is the relative influence of cluster i for the hour of trajectory arrival t, C_i is the set of all cells assigned to cluster i, C_n is the set of all cells in the grid ($C_i \subseteq C_n$), $n_k(t)$ is the total number of pixel piercings for cell k by any of the nine trajectories arriving simultaneously at CHC at hour t, and w_k is the relative weight of cell k as a function of mean residence time and distance to CHC.

Air masses arriving at CHC are usually composed of a mix of the six clusters, and in only very few cases the relative influence of one single cluster reaches 100%. Thus, we applied a selection threshold to assign hourly measurements at CHC to one single cluster: If the percentage of relative cluster influence as calculated by Eq. (1) exceeded the selection threshold for any of the six clusters, we considered the latter to be the "dominant cluster" and assigned to it alone all measurements taken at CHC during the hour of back trajectory arrival. All data obtained at arrival times for which none of the clusters was dominant were excluded from this analysis. Unless stated otherwise, we chose a threshold of 70% to find a compromise between unambiguousness of air mass origin and data availability, as the latter decreases rapidly with higher selection thresholds, especially for the weaker clusters C2, C3, C4, and C6. In a nutshell, if the set of nine back trajectories arriving simultaneously at the station spent over 70% of its time within cells assigned to one single cluster, we considered the latter to be the "dominant cluster" (at a selection threshold of 70%).

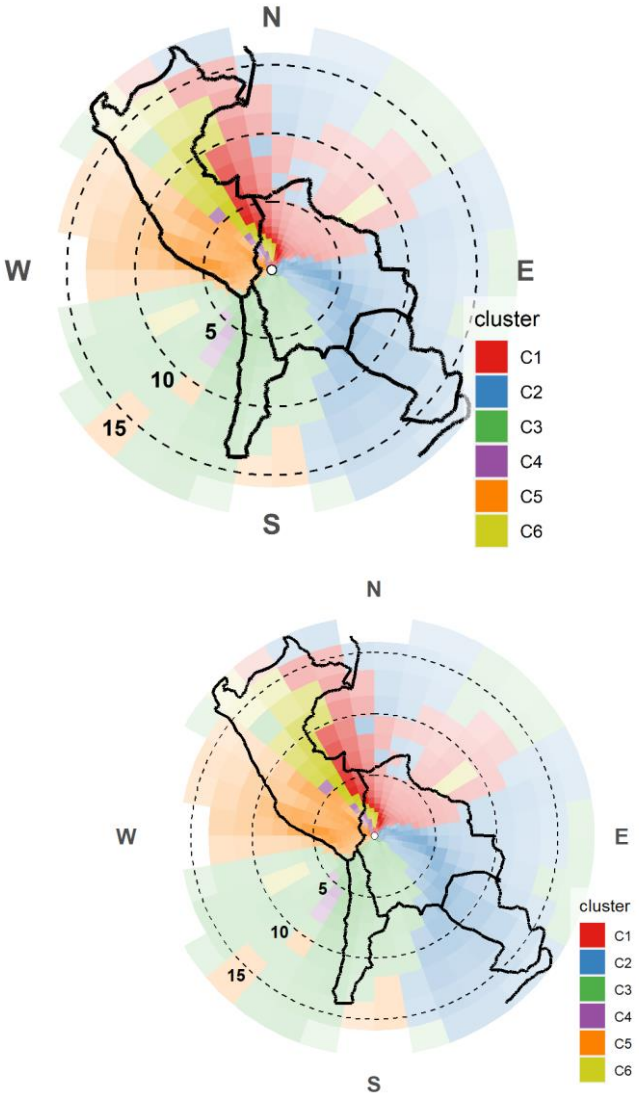

Fig. 2: Air mass cluster definition as obtained by Chauvigné et al. (2019). Log-polar coordinate system, centered on CHC (white dot). Cells shaded according to the square root of weight, which is a function of residence time and distance to CHC. Dashed range circles show the distance ~~Distance~~ to CHC in degrees, convertible to km by using the conversion factor 1° = 108.6 km, with an error below 3% ~~is shown~~ in the whole domain. ~~dashed range circles.~~ Black lines show the borders among countries.

2.5 Pollution maps

To further visualize the link between air mass origin and TGM concentrations, we produced what we call "pollution maps". These are based on the same set of HYSPLIT back trajectories introduced previously, and were computed with the following procedure: First, for each single back trajectory, we assigned the TGM concentration at back trajectory arrival to each of its endpoints (each back trajectory consists of 96 trajectory endpoints, one for every hour of its runtime). Then we defined a geographical grid and grouped together all endpoints (defined in space by latitude, longitude, and elevation over ground level) falling into the same grid cell. Finally, for each grid cell, we calculated the arithmetic mean of all TGM concentrations assigned to the corresponding grouped endpoints.

It has to be highlighted that this procedure permits the multiple counting of the same measured TGM concentration in the calculation of one single grid cell mean. This happens if more than one endpoint of the same trajectory or endpoints of different trajectories with the same arrival time fall into the same geographical grid cell. We considered this sort of inherent weighting to be desirable, as it gives greater weight to TGM concentrations assigned to air masses passing an extended period of time over the grid cell in question. However, to assure a certain degree of statistical significance, we excluded those grid cell means based on less than 10 independent data points on TGM concentration ($n < 10$).

To account for growing trajectory uncertainty with increasing distance to the receptor site (CHC), avoid the misinterpretation of a pollution map as a satellite image, and allow for the easy visual comparison between pollution maps and air mass clusters, we used the exact same CHC centered log-polar grid as deployed in Chauvigné et al. (2019).

With the goal of focusing on potential sources and sinks acting close to the surface, we excluded all trajectory endpoints with an elevation greater than 1000 m a.g.l from this analysis (assuming an average boundary layer height of 1000 m a.g.l). This means essentially that only trajectories passing at low altitudes over a grid cell have an influence on the TGM average calculated for the cell.

3. Results

3.1 TGM concentrations in normal and ENSO conditions, seasonality

A summary of the monthly averaged TGM concentrations is presented in Fig. 3a. The data shows an overall rising trend during the measurement period. As this trend exhibits a striking similarity to the evolution of the ONI index (Fig. 3c), we suggest an important ENSO influence on TGM measured at CHC. This will be discussed in detail in an upcoming publication. In the present paper, we labelled the last nine months of our measurement period (June 2015 - Feb 2016) with ONI > 1 as ENSO conditions (EC) and excluded them from most of our analysis as not representative of normal conditions (NC).

We obtained a mean TGM concentration of $0.89 \pm 0.01\, ng\, m^{-3}$ for NC and a significantly higher mean of $1.34 \pm 0.01\, ng\, m^{-3}$ for EC ($p < 2.2 \cdot 10^{-16}$, Mann-Whitney test). For both NC and EC, we can observe a similar seasonal pattern, with low TGM concentrations during the dry season, rising TGM concentrations during

BB season, and highest TGM concentrations at the beginning of the wet season (Fig. 3a and Fig. 3b). In the case of NC, TGM concentrations started declining again in January, while this was not observable for EC.

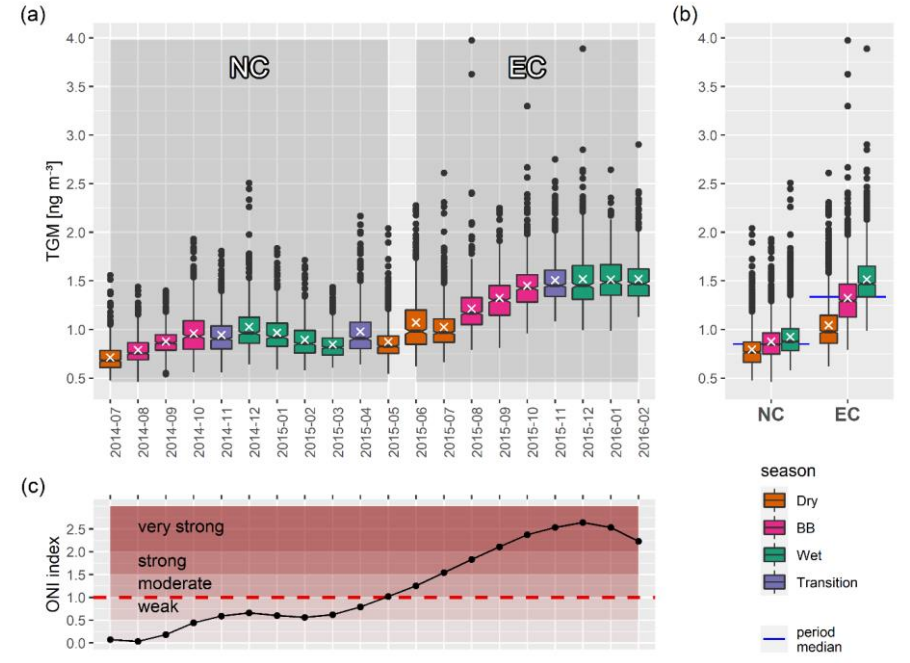
(a)
NC
EC
TGM [ng m-3]
4.0
3.5
3.0
2.5
2.0
1.5
1.0
0.5
2014-07
2014-08
2014-09
2014-10
2014-11
2014-12
2015-01
2015-02
2015-03
2015-04
2015-05
2015-06
2015-07
2015-08
2015-09
2015-10
2015-11
2015-12
2016-01
2016-02
(b)
NC
EC
(c)
ONI index
very strong
strong
moderate
weak
season
Dry
BB
Wet
Transition
period
median

357

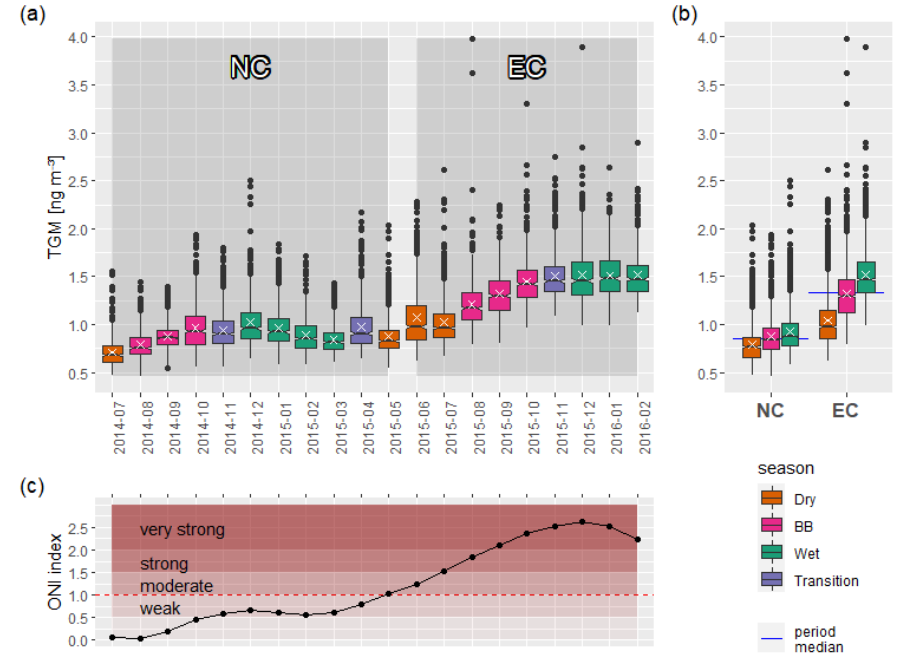
(a)
NC
EC
TGM [ng m-3]
4.0
3.5
3.0
2.5
2.0
1.5
1.0
0.5
2014-07
2014-08
2014-09
2014-10
2014-11
2014-12
2015-01
2015-02
2015-03
2015-04
2015-05
2015-06
2015-07
2015-08
2015-09
2015-10
2015-11
2015-12
2016-01
2016-02
(b)
NC
EC
(c)
ONI index
very strong
strong
moderate
weak
season
Dry
BB
Wet
Transition
period
median

358

Fig. 3: (a) Time evolution of TGM at CHC during the entire measurement period. Notches display 95% confidence intervals for the median, means are shown as white crosses, "normal conditions" (NC) and "ENSO conditions" (EC) time intervals as shaded boxes. Whiskers extend until the highest/lowest data point within the interval [1st quartile – 1.5 IQR, 3rd quartile + 1.5 IQR], values outside that range are shown as black dots. (c) Evolution of the ONI index during the same period alongside NOAA definitions on the strength of ENSO phases. The dashed red line shows the boundary value we used here to separate NC from EC (ONI = 1). (b) Seasonality of TGM in CHC during NC and EC, transition months excluded. Horizontal blue lines show the total median of the respective period.

3.2 Diel cycle, urban influence and nearby contamination

Given that the metropolitan area of La Paz/El Alto is located less than 20 km downhill of the measurement site, we investigated the possibility of a statistically important urban influence on TGM measurements. Previous studies (Andrade et al., 2015, Wiedensohler et al., 2018) have shown a significant influence of regional sources and the nearby metropolitan area on CO and eBC concentrations measured at the station. A marked increase in average CO and eBC diel patterns (Fig. 4b and Fig. 4c), starting at around 9:00 local time, has been linked to the arrival of the Altiplanic planetary boundary layer, vehicle traffic, and urban contamination in general. In contrast, the diel cycle of TGM (Fig. 4a) is qualitatively different, with no marked increase associated to the arrival of the boundary layer, but instead slightly lower TGM values between about 7:00 and 19:00 local time, which coincides well with the typical hours of sunlight and generally boundary layer influence. The absence of a diel pattern driven by traffic and urban pollution is not very surprising, since there are no major sources of mercury in the poorly industrialized cities of La Paz and El Alto, and domestic heating is nearly absent. The only potential local sources we suggest could be the occasional waste burning by individuals and a cement factory located at about 40 km to the southwest of the station (Cemento Soboce, 16°38'49.2"S 68°19'01.2"W, Fig. 1). Either way, the magnitude of urban or traffic-related TGM contamination at CHC appears to be negligible.

Still, one event where TGM concentrations were clearly driven by nearby anthropogenic pollution was Saint John's Eve, the night between the 23rd and 24th of June 2015, where TGM concentrations peaked alongside CO and eBC concentrations (Fig. 4d, Fig. 4e, Fig.4f). During nights around that traditional festivity, numerous bonfires are lit and fireworks are launched in the region. In the bonfires, not only untreated wood is used for combustion, but also garbage, old furniture, and other objects. The relatively high mean TGM concentrations during June 2015, as compared to May and July 2015 (Fig. 3a), could be explained by the Saint John event alone, especially if we consider the relatively poor data coverage during that month (only 21 out of 30 daily averages available) and the resulting greater weight given to a few days (~ 6 days) of elevated concentrations.

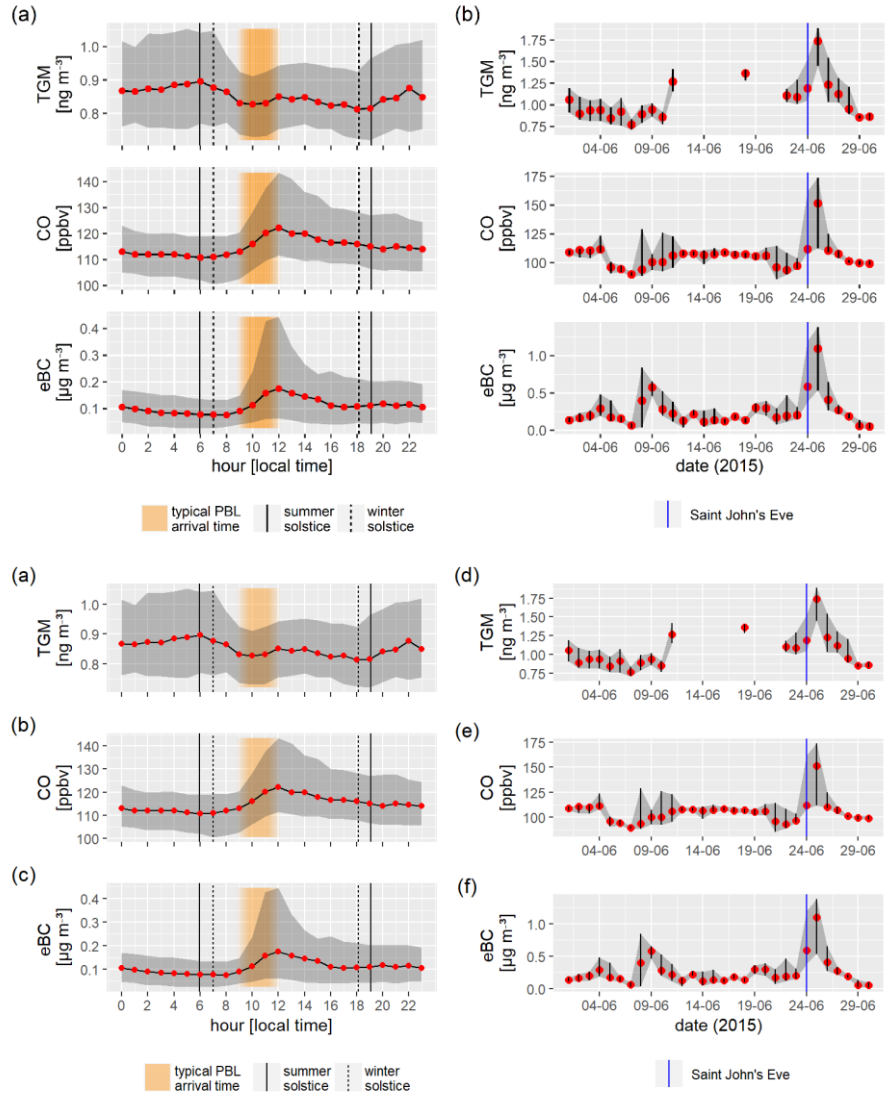

Fig. 4, Left: Median diel cycles of (a) TGM, (b) CO, and (c) eBC for NC. Limits of grey shaded area correspond to the 25th and 75th percentile. Vertical lines represent sunrise and sunset hours for the summer solstice in the wet season (solid line) and the winter solstice in the dry season (dashed line). The typical arrival time of the urban-influenced Altiplanic planetary boundary layer (PBL) is highlighted in orange. Right: Daily averaged (25th percentile, median, 75th percentile) (d) TGM, (e) CO, and (f) eBC during June 2015.

Formatted: Font: 10 pt, Italic, Check spelling and grammar

3.3 Spatial differences of TGM concentrations, air mass origin

The evident seasonal pattern in transportation pathways towards CHC is visualized in Fig. 5. The most important air mass clusters during NC, measured by mean relative influence and appearance as the dominant cluster, were Amazonian C1 and Altiplanic C5 (Fig. 5c and Fig. 5d).

In the dry season, most of the air masses arriving at the station were western Altiplanic (C5), passing over the Peruvian highlands and the Titicaca lake. This changed in the wet season with a clear shift towards predominantly Amazonian/lowland air masses (northerly C1 and easterly C2). The Altiplanic cluster C5 was weak during that time of the year (mean relative influence < 10%).

With much less seasonal variation, southerly Altiplanic air (Cluster C3) arrived occasionally from the border between Bolivia and Chile after passing through parts of the CVZ and - frequently - the urban area of La Paz/El Alto. Altiplano/lowland interface clusters C4 and C6 were relatively weak throughout the year and appeared very infrequently as dominant clusters at a threshold of 70% (Fig. 5d).

As shown in Fig. 6, we tried to infer potential source and sink regions of TGM through clustering results and a pollution map (based on an endpoint cutoff altitude of 1000 m a.g.l, as described in the methodology section; pollution map results at different cutoff altitudes can be consulted in Appendix B). Based on all NC data, Northern Amazonian and Southern Altiplanic air masses, especially those passing over or close to reportedly degassing volcanoes south of CHC (Ollague, San Pedro, Putana, Lascar, Lastarria; Tamburello et al., 2014; Tassi et al., 2011), carried the highest mean TGM concentrations (around $0.94 \pm 0.02\ ng\ m^{-3}$ and $1.08 \pm 0.08\ ng\ m^{-3}$ respectively), while western Altiplanic and south-eastern lowland air masses showed the lowest mean TGM concentrations (around $0.80 \pm 0.02\ ng\ m^{-3}$ and $0.85 \pm 0.02\ ng\ m^{-3}$ respectively, Fig. 6a). By grouping data by season (i.e. wet, dry, and BB), more detailed information could be extracted (Fig. 6b). Only the Northern – Amazonian cluster C1 showed both the highest CO and TGM concentrations during the BB season (arithmetic means of $150 \pm 5\ ppbv$ and $0.99 \pm 0.04\ ng\ m^{-3}$ respectively). Western Altiplanic cluster C5 exhibited the lowest mean TGM concentrations in the dry season ($0.77 \pm 0.01\ ng\ m^{-3}$) and the highest TGM concentrations in the wet season ($0.93 \pm 0.07\ ng\ m^{-3}$). The mean concentration in southern-Altiplanic cluster C3 was $0.92 \pm 0.05\ ng\ m^{-3}$ with no significant differences between the wet and BB season ($p = 0.76$, Mann-Whitney test). Eastern lowland cluster C2 did only contribute as a dominant cluster during the wet season, but showed by far the lowest mean TGM concentrations during that time of the year ($0.82 \pm 0.02\ ng\ m^{-3}$). The seasonal change in transport pathways becomes evident if we consider that in the dry season, only Altiplanic C5 contributed significantly as a dominant cluster (at a selection threshold of 70%). No useful information could be extracted about altiplano-lowland interface clusters C4 and C6, as their relative influence throughout the year was low (Fig. 5c and Fig.5d).

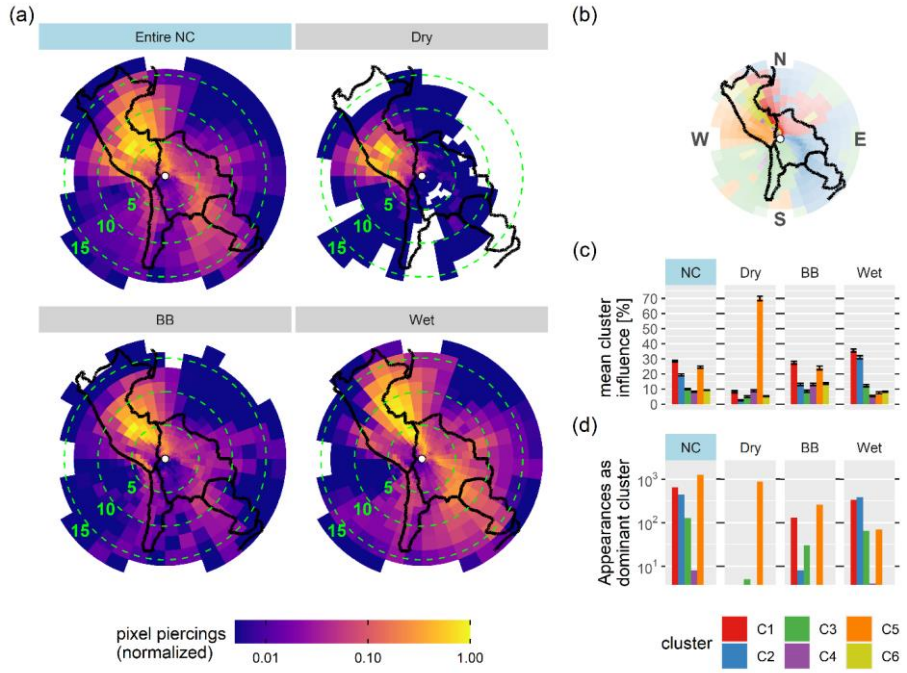
(a)
Entire NC
Dry
BB
Wet
5
10
15
pixel piercings
(normalized)
0.01
0.10
1.00
(b)
N
W
E
S
(c)
NC
Dry
BB
Wet
mean cluster
influence [%]
70
60
50
40
30
20
10
0
(d)
Appearances as
dominant cluster
10^3
10^2
10^1
cluster
C1
C2
C3
C4
C5
C6

431

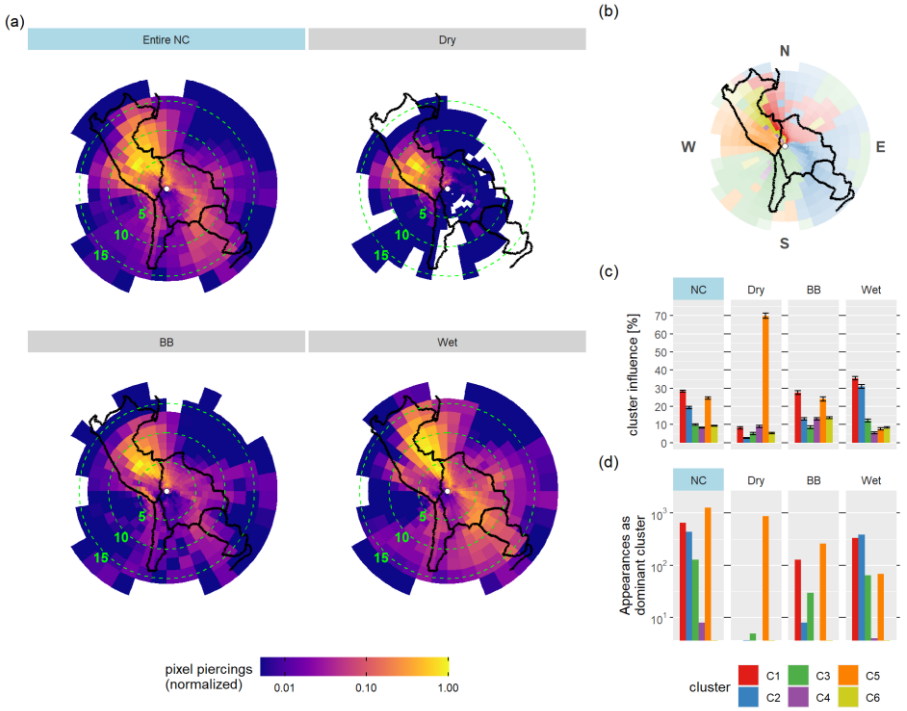

Fig. 5: (a) Total number of back trajectory piercings per pixel for NC and its seasons, normalized through division by the maximum, so that "1" corresponds to the most frequently pierced pixel. Note the logarithmic color scale. The polar grid has constant angular, but variable radial resolution and is centered on CHC (white dot). Dashed range circles show the distance ~~Distance~~ to CHC in degrees, convertible to km by using the conversion factor 1° = 108.6 km, with an error below 3% ~~is shown~~ in the whole domain. ~~dashed circles.~~ Right: (b) Reminder of the cluster definition as obtained by Chauvigné et al. (2019), using the same polar grid. (c) Weighted mean relative influence (%) for the six clusters during the entire NC and its seasons. (d) Number of cluster appearances as "dominant cluster" at a threshold of 70%. Note the logarithmic y-axis.

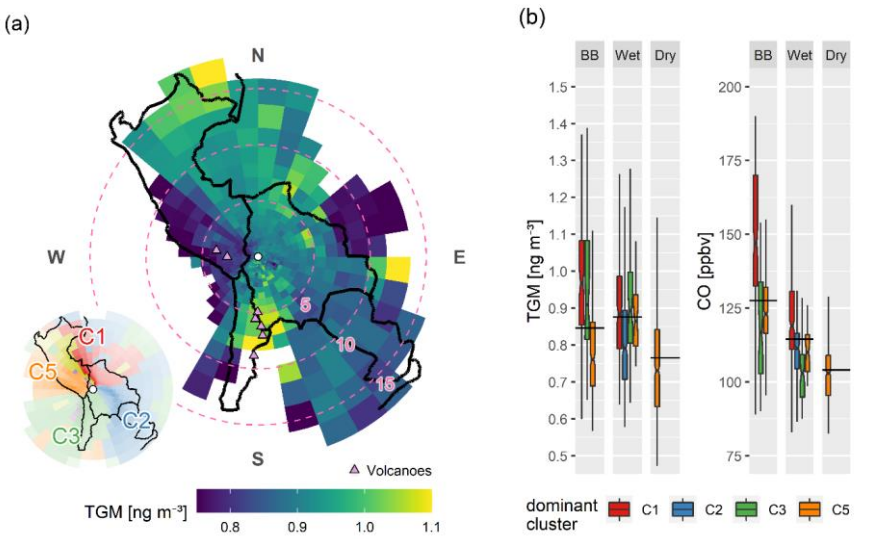

441

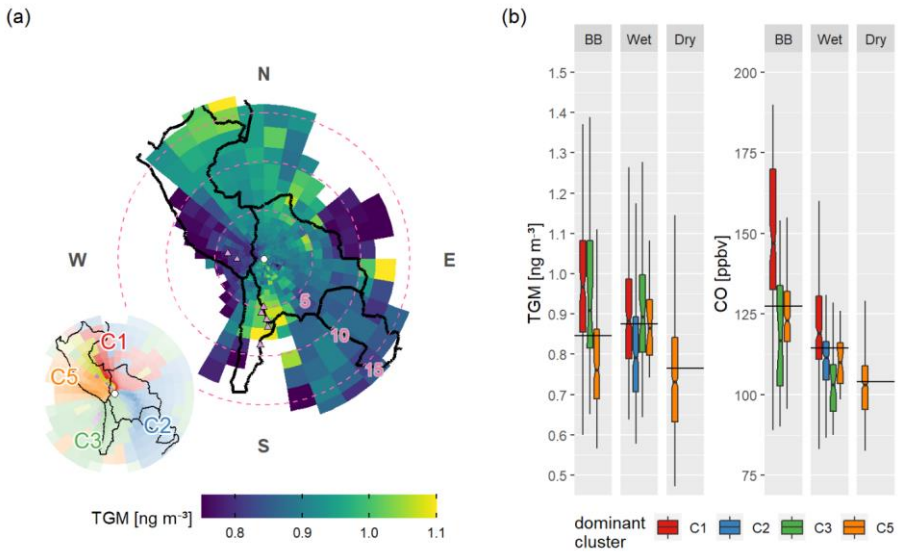

442

443 *Fig. 6: (a) Pollution map based on TGM data taken during the entire NC. Polar grid is centered on CHC (white*
444 *dot). Dashed range circles show the distance~~Distance~~ to CHC in degrees, convertible to km by using the*
445 *conversion factor 1° = 108.6 km, with an error below 3%~~ is shown~~ in the whole domain.~~ dashed range circles.~~*
446 *Trajectory endpoints with an elevation > 1000 m a.g.l. and cells with less than 10 data points (n < 10) were*
447 *excluded. Color scale capped at the limits. Pink triangles show selected degassing volcanoes in the CVZ, from*
448 *north to south: Sabancaya, Ubinas, Ollague, San Pedro, Putana, Lascar, Lastarria. The small map shows the*

air mass cluster definition. (b) TGM and CO concentrations for different seasons and clusters during NC, based on a cluster selection threshold of 70%. Groups~~Outliers and groups~~ with n < 10 are excluded from~~not shown in~~ the plot. Horizontal lines show seasonal medians based on all NC data. Whiskers extend until the highest/lowest data point within the interval [1st quartile – 1.5 IQR, 3rd quartile + 1.5 IQR], values outside that range are not shown.

4. Discussion

4.1 TGM means and seasonality

TGM concentrations during NC (11-month mean from July 2014 to May 2015: $0.89 \pm 0.01\ ng\ m^{-3}$) were about 10% to 15% lower, compared to subtropical sites of the Southern Hemisphere such as Amsterdam Island in the remote southern Indian Ocean (37.7983 S - 77.5378 E, 55 m a.s.l) with a GEM annual mean of $1.034 \pm 0.087\ ng\ m^{-3}$ (from 2012 to 2017; Angot~~Slemr~~ et al., 2014; Slemr et al., ~~-~~ 2020) and the Cape Point GAW station in South Africa (34.3523 S - 18.4891 E, 230 m a.s.l) with a GEM annual mean around $1\ ng\ m^{-3}$ (from 2007 to 2017; Martin et al., 2017; Slemr et al., 2020). No GEM annual mean below $1\ ng\ m^{-3}$ was observed in these two atmospheric mercury monitoring stations in 2014 and 2015, corresponding to the CHC NC period. Mean annual GEM concentrations of $0.95 \pm 0.12\ ng\ m^{-3}$, i.e. close but still higher than the NC TGM concentrations, were observed from 2014 to 2016 (Howard et al., 2017) at the Australian Tropical Atmospheric Research Station (ATARS) in Northern Australia (12.2491 S - 131.0447 E, near sea level) while the mid-latitude Southern Hemisphere site of global GAW Cape Grim (40.683 S – 144.689 E, 94 m a.s.l) exhibited annual mean concentrations around $0.86\ ng\ m^{-3}$ (from 2012 to 2013; Slemr et al., 2015). TGM concentrations at CHC are well in line with measurements on the continent performed at Titicaca lake, at around 3800 m a.s.l and about 60 km west from our site (not continuously measured between 2013 and 2016: TGM mean of $0.82 \pm 0.20\ ng\ m^{-3}$ in the dry and $1.11 \pm 0.23\ ng\ m^{-3}$ in the wet season; Guédron et al., 2017) and in Patagonia (from 2012 to 2017, GEM mean of $0.86 \pm 0.16\ ng\ m^{-3}$, Diéguez~~Dieguez~~ et al., 2019).

CHC TGM during NC showed a marked seasonality, with lowest TGM during the dry season ($0.79 \pm 0.01\ ng\ m^{-3}$), increasing values during BB season ($0.88 \pm 0.01\ ng\ m^{-3}$) and highest TGM during the wet season ($0.92 \pm 0.01\ ng\ m^{-3}$). This behaviour is congruent with the results from Guedrón et al. (2017), even though the seasonal difference did not appear statistically significant for the latter. The marked seasonality at the CHC site is in contrast to what has been observed at some subtropical and mid-latitude sites in the Southern Hemisphere, both in terms of the amplitude and the seasonal average level (Howard et al., 2017; Slemr et al., 2015, 2020).

This seasonality is likely a product of the superposition of several important drivers, coupled with seasonal changes in transportation pathways (Fig. 5). In the next sections, we further explore the potential role of BB related Hg emissions, the Amazon rainforest, and the Pacific Ocean. We also explore volcanoes in the CVZ and ASGM as atmospheric Hg sources without specific seasonality but with possible influence on CHC TGM levels.

4.2 Biomass burning and TGM/CO emission ratio

4.2.1 Biomass burning influence

BB is an important source of atmospheric mercury (Obrist et al., 2018; Shi et al., 2019). Friedli et al. (2009) estimated global mercury emissions from BB and found a high contribution from South America ($13 \pm 10\, Mg_{Hg}\, yr^{-1}$ for its northern hemispheric and $95 \pm 39\, Mg_{Hg}\, yr^{-1}$ for its southern hemispheric part). Michelazzo et al. (2010) measured Hg stored in Amazonian vegetation before and after fires, finding that mercury emissions originated mostly from the volatilization of aboveground vegetation and the plant litter layer (O-horizon). Very recently Shi et al. (2019) showed, among others, high Hg emissions in northern Bolivia, a region overlapping very well with the source region of Amazonian cluster C1. Indeed, for this cluster, whose BB influence was already confirmed by Chauvigné et al. (2019), we found both the highest CO and TGM concentrations during the BB season (compare to Fig. 6b and Fig. A1), in both cases significantly higher than during the rest of the NC ($p < 2.2 \cdot 10^{-16}$ and $p < 0.0008$ respectively, Mann-Whitney test).

In order to further explore the link between BB and TGM in our data, independently of computed HYSPLIT back trajectories, we used the combination of in situ measured CO and eBC data as tracers for distinct combustion sources and transport times (Choi et al., 2020; Subramanian et al., 2010; Zhu et al., 2019). We grouped CO and eBC data into eight percentile groups each, ranging from 0th to 100th in steps of 12.5% (CO range: $37 \rightarrow 336\ ppbv$; eBC range: $0 \rightarrow 5.09\ \mu g\, m^{-3}$). Based on these groups we produced an 8x8 grid, where each cell ("pollution signature") corresponds to a combination of CO and eBC concentration intervals. We then calculated the median TGM concentration for each pollution signature in the grid (Fig. 7a).

Pollution signatures showed a clear seasonal trend. During the dry season, eBC was tendentially high and CO low. TGM concentrations tended to increase with rising CO concentrations, while even highly eBC enriched air masses had very low TGM concentrations in the absence of CO (for example, cells B-8, C-8). The latter suggests that urban pollution originating from traffic does not act as an important driver of atmospheric Hg measured at CHC, in agreement with the TGM diel pattern (Fig. 4a), which shows no TGM increase upon arrival of the frequently traffic influenced planetary boundary layer and a simultaneous increase in eBC. During the wet season, eBC at CHC station was tendentially very low, which is likely linked to the increased wet deposition of particulate matter during that season, while CO concentrations were very variable. The absence of a visible pattern concerning TGM in those pollution signatures suggests that TGM concentrations during the wet season are either not importantly affected by combustion of any kind, or that around this time different combustion sources are indistinguishable through their eBC and CO signatures.

Finally, BB season pollution signatures generally showed very high CO and highly variable eBC concentrations. Within those signatures, TGM concentrations clearly increased with rising CO concentrations but did not depend strongly on eBC loadings, even though they tended to be lower in the case of very low eBC (example: H1, H3, G3, F3. Exception: H2).

Considering that atmospheric lifetime is much shorter for BC than for CO (days - weeks for BC, Cape et al., 2012; Park et al., 2005; months for CO, Khalil et al., 1990), especially under conditions of high wet deposition, we can expect that even if both eBC and CO are strongly co-emitted during BB events, air masses arriving at CHC should be significantly enriched in CO only after a few days of transport. We can thus interpret the steadily high CO but comparatively low eBC loading of air masses with these pollution signatures as the result of an important BC

deposition (wet and dry) during the transport between pollutant source and receptor side regions, either due to precipitation favoring wet deposition or a transport time of at least a few days. As the metropolitan area of La Paz/El Alto, a hotspot for BC (Wiedensohler et al., 2018), is quite close to the station (< 20 km) and transport time is therefore usually less than a few hours (compare to Fig. C1 in Appendix C), we can exclude urban influences as contributors to these pollution signatures and assign them to BB.

As median TGM concentrations were significantly higher in those pollution signatures occurring almost exclusively in the BB season (over 85% of the time, Fig. 7a), compared to median NC concentrations ($0.93\,ng\,m^{-3}$ vs. $0.85\,ng\,m^{-3}$, $p = 1.7 \cdot 10^{-11}$, Mann-Whitney test), we can conclude that there is an important influence of regional and continental BB on atmospheric mercury concentrations in the Bolivian Andes. This occurs only during a few months of the year (August - October) and it is mostly constrained to northern-Amazonian air masses (cluster C1, remotely obtained CO concentrations in the cluster C1 source region are shown in Appendix A).

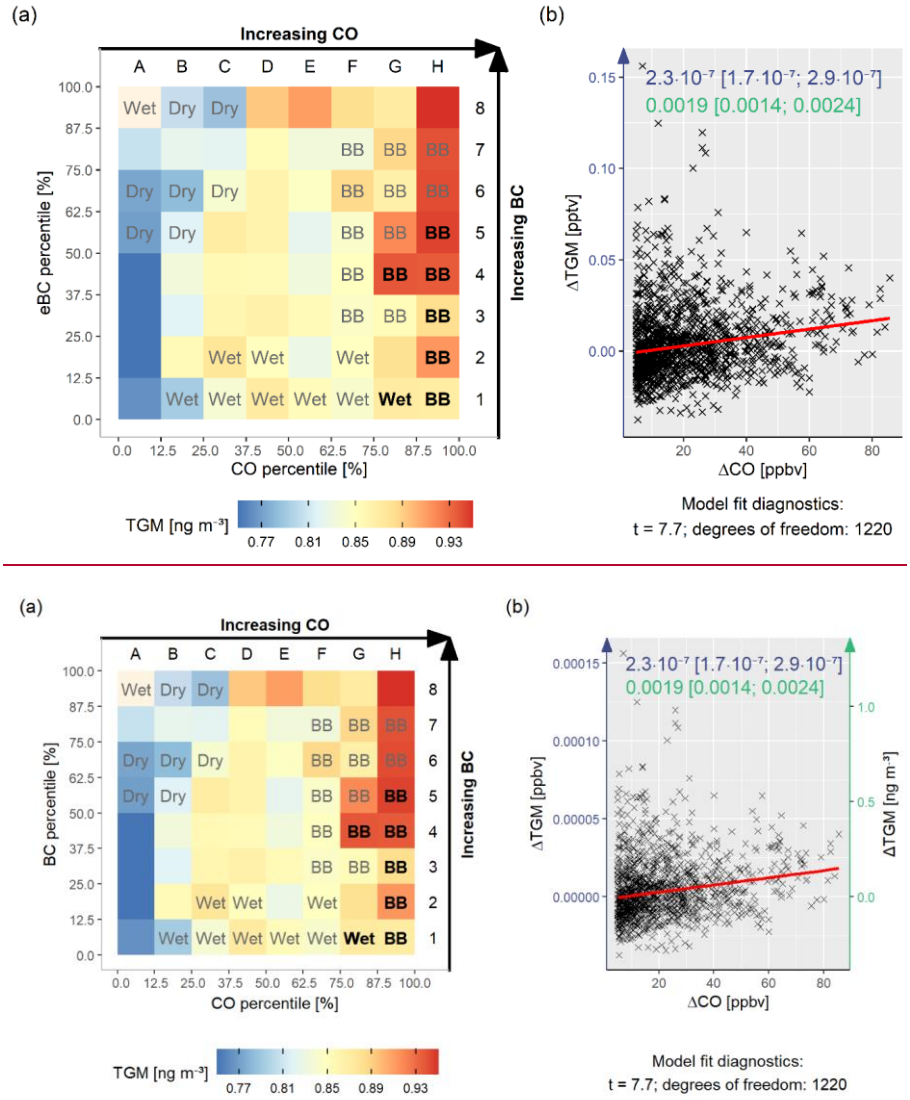

Fig. 7: (a) TGM medians for different combinations ("pollution signatures") of eBC and CO concentrations, each split into 8 percentile groups ranging from 0 to 100%, so that the first group contains data below the 12.5th and the last group data above the 87.5th percentile. All data were taken during NC at CHC. Grey (black) letters mark signatures whose data falls into the respective season more than 51% (85%) of the time. Cells with n <30 shaded out proportionally. Color scale centered on NC median and capped at the limits. (b) Red line shows robust linear model (iteratively reweighted least squares) between ΔTGM and ΔCO, defined as the difference between actual measurement and assumed background concentrations, for all data in pollution signatures with a >51% occurrence during NC BB season (all cells with grey or black "BB" letters in (a)). The resulting slope, which can

be interpreted as TGM/CO emission ratio, is given in units of $ppbv_{TGM}\ ppbv_{CO}{}^{-1}$ *(blue) and* $(ng\ m^{-3})_{TGM}\ ppbv_{CO}{}^{-1}$ *(green) with its 95% confidence interval.*

4.2.2 TGM/CO emission ratio

Having established a clear link between TGM and long-range transported BB in our data, we aimed to estimate an average biomass burning TGM/CO emission ratio on the continent. A first obstacle arises from the fact that BB is not the only source for TGM and CO measured at Chacaltaya. CO in particular is also readily emitted by anthropogenic activities (e.g. urban, traffic) in the surrounding Altiplano, as can be inferred from CO diel patterns (Fig. 4b) and previous work (Wiedensohler et al., 2018). In consequence, simply computing TGM vs. CO in the entire unfiltered CHC dataset would not provide the biomass burning related TGM/CO emission ratio, but a sort of "net emission ratio" over different sources of pollution with distinct emission ratios. To remove this distorting factor as much as possible and obtain a "best guess" biomass burning TGM/CO emission ratio, we used the results from the previous section ("pollution signatures"): We attempted to isolate highly BB influenced air masses by selecting only data with pollution signatures occurring preferentially during the BB season (> 51% of signature data taken in BB season, Fig.7, left) as BB representatives.

With this data selection performed, a linear model between TGM and CO could not yet be computed directly to obtain the emission ratio, as this would assume constant TGM and CO background conditions for the whole data selection. This is not a valid assumption, considering that the selection contains TGM data from different months and that a strong seasonal pattern was observed (Fig. 3a and Fig. 3b). To account for the changing background conditions, we first computed ΔTGM and ΔCO, which we defined as their measured concentration minus their assumed background concentration at the time of measurement. We expressed the TGM background through a 30-days running median, as it is clearly not constant during the year and seasonally shifting concentrations cannot be attributed to BB only. This is different for CO, where we can assume that BB is the main driver of the seasonal signal in South America (Fig. A1a) and that the BB-unrelated fluctuations in background concentrations are small in comparison to the BB induced variations in measured concentrations at CHC (Fig. A1b). We thus used a simple median using all NC data to express the CO background (Illustrated in Fig. A1b).

Finally, we determined the TGM/CO emission ratio through the use of a robust linear regression (linear regression with iterative reweighting of points) between ΔTGM and ΔCO ($\Delta TGM = a + b \cdot \Delta CO$), obtaining a slope of $(2.3 \pm 0.6) \cdot 10^{-7} ppbv_{TGM}\ ppbv_{CO}{}^{-1}$ (Fig. 7b). This obtained emission ratio is robust towards changes in the parameters chosen for its calculation (Sensitivity analysis presented in Appendix D), and is in good agreement with previous results. Ebinghaus et al. (2007) deduced TGM/CO emission ratios of $(1.2 \pm 0.2) \cdot 10^{-7}\ ppbv_{TGM}\ ppbv_{CO}{}^{-1}$ and $(2.4 \pm 1) \cdot 10^{-7}\ ppbv_{TGM}\ ppbv_{CO}{}^{-1}$ during CARIBIC flights over Brazil through measurements performed directly within fire plumes. Weisspenzias~~Penzias~~ et al. (2007), using a more similar approach to ours, obtained results ranging from $(1.6 \pm 1) \cdot 10^{-7}\ ppbv_{TGM}\ ppbv_{CO}{}^{-1}$ for air massing originating in Pacific Northwest US up to $(5.6 \pm 1.6) \cdot 10^{-7}\ ppbv_{TGM}\ ppbv_{CO}{}^{-1}$ for those originating in industrial East Asia (*numbers converted from* $(ng\ m^{-3})_{TGM}\ ppbv_{CO}{}^{-1}$ *to* $ppbv_{TGM}\ ppbv_{CO}{}^{-1}$).

We observe a high scatter around our regression line of best fit, which is not surprising, considering the distance from the receptor site to the source region and the resulting dilution and mixing. Due to that, our data pairs of TGM and CO do not correspond to the emissions of one single fire event, but many different fires and plumes and

589 also distinct times and conditions of aging. The obtained emission ratio should thus be interpreted as an average
590 emission ratio of all fires in the northern Bolivian lowlands and the Amazon, after some aging has occurred.

591 **4.3 The potential role of the vegetation in the TGM cycle**

592 Globally, the role of vegetation in the mercury cycle is not yet completely understood, but there is much evidence
593 pointing towards both reactive mercury (RM) deposition on leaf surface and a direct vegetation uptake of GEM.
594 However, as highlighted in the literature review by Obrist et al. (2018), these pathways, especially the latter, are
595 still not well constrained. Recently, Jiskra et al. (2018), reported a significant correlation between the remotely
596 sensed vegetation tracer NDVI (normalized difference vegetation index) and GEM levels for individual sites in
597 the Northern Hemisphere and argued that the absence or weakness of Hg seasonality in many sites of the Southern
598 Hemisphere might be linked to its comparatively lower landmass and lesser vegetation uptake. A similar point
599 was made earlier by Obrist (2007), who proposed that vegetation uptake in the Northern Hemisphere might be
600 partly responsible for the observed TGM seasonality in Mace Head, Ireland, a hypothesis based on the correlating
601 seasonal patterns of atmospheric TGM and CO_2. Indeed, Ericksen~~Eriksen~~ et al. (2003~~2002~~) showed in mesocosm
602 experiments that foliar Hg concentrations in gas chambers increase over time, levelling off after 2-3 months. They
603 furthermore reported that roughly 80% of the total accumulated Hg was stored in leaf matter and that soil Hg
604 levels in the mesocosms had no significant effect on foliar Hg concentration, a piece of strong evidence that Hg
605 is taken up directly from the atmosphere and not from the soil. Some very similar points were made by Grigal
606 (2003), based on a review of Hg concentrations in forest floors and forest vegetation. Although it is assumed that
607 vegetation acts as a net sink for atmospheric mercury (Obrist et al., 2018), Yuan et al. (2019) studied mercury
608 fluxes in a subtropical evergreen forest and found isotopic evidence for a GEM re-emission process within leaves,
609 counteracting partly the GEM uptake. They also reported a strong seasonality in mercury fluxes, with the highest
610 GEM uptake in the growing / wet season. Considering these previous results, a modulation of continental-wide
611 Hg levels through the Amazon rainforest is likely. Indeed, Figueiredo et al. (2018) already suggested that the
612 Amazon rainforest acts as a net sink for atmospheric mercury, based on forest soil profiles.

613 To address such a possible link between TGM and vegetation in our data, we focused on lowland air masses only,
614 as vegetation coverage in the altiplano is sparse, GPP is low and consequently no important vegetation sink effect
615 is to be expected in Altiplanic air masses. Although both clusters C1 and C2 would qualify as lowland clusters
616 passing over evergreen forests, C2 did not provide enough data to compute a useful series of monthly averages.
617 Therefore, we selected Amazonian cluster C1 as the sole representative of Amazonian air masses. We explored
618 two different proxies for a possible vegetation sink effect: CO_2 concentrations measured at CHC (detrended,
619 assuming a Southern Hemisphere linear trend of 2 ppm/year; trend based on AIRS CO_2 data between January
620 2010 and January 2015, averaged over whole South America) and satellite obtained solar induced fluorescence
621 (SIFTER) averaged over the (legal) Amazon rainforest as a proxy for amazon GPP. We then computed the slope
622 of robust linear models for the combinations TGM vs. CO_2 $(TGM = a + b \cdot CO_2)$ and TGM vs. SIFTER
623 $(TGM = a + b \cdot SIFTER)$ for C1 dominant air masses at increasing selection thresholds.

624 We observe an interesting trend, where the magnitude of the slopes becomes more important and slope uncertainty
625 (compare to Sect. 2.2.6, "Uncertainties and confidence intervals") decreases with an increasing Amazonian cluster
626 C1 selection threshold (Fig. 8a and Fig. 8b). For thresholds of 70% and 80%, the resulting TGM vs. CO_2 slopes

are $0.047\ [0.035; 0.060]$ and $0.058\ [0.041; 0.075]\ (ng\ m^{-3})_{TGM}\ ppm_{CO2}{}^{-1}$ respectively, while the resulting TGM vs. SIFTER slopes are $-0.82\ [-1{,}11; -0.53]$ and $-1.51\ [-2.05; -0.97]\ (ng\ m^{-3})_{TGM}\ (mW\ sr^{-1}m^{-2}nm^{-1})_{SIF}{}^{-1}$. Closer inspection of the corresponding TGM, CO_2, and SIFTER monthly averages at a C1 threshold of 70% visualizes how both TGM and CO_2 reached their minimum in March 2015, coinciding with a peak of Amazon SIFTER as a proxy for Amazon GPP (Fig. 8d, Fig. 8e, Fig. 8f).

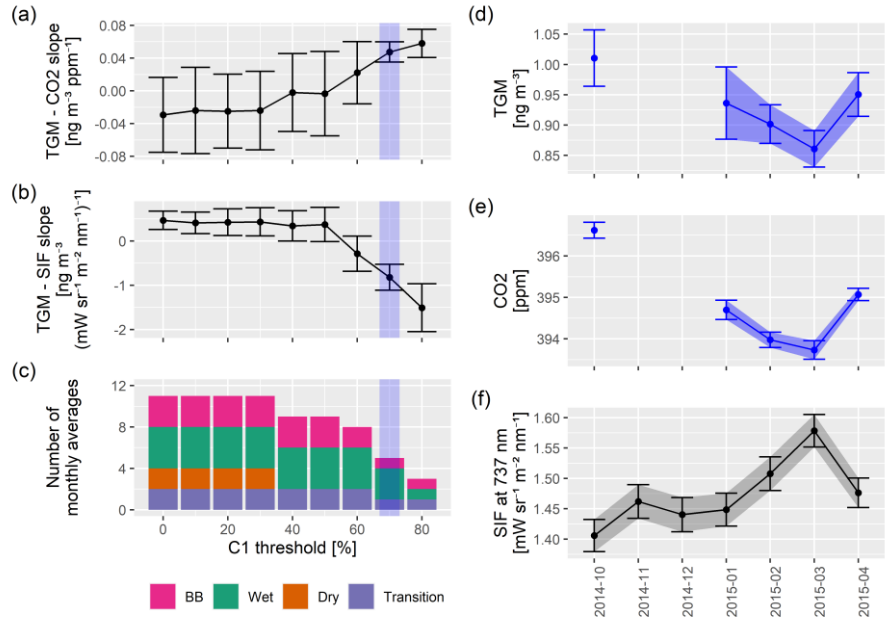
(a)
TGM - CO2 slope [ng m-3 ppm-1]
0.08
0.04
0.00
-0.04
-0.08
(b)
TGM - SIF slope [ng m-3 (mW sr-1 m-2 nm-1)-1]
0
-1
-2
(c)
Number of monthly averages
12
8
4
0
0
20
40
60
80
C1 threshold [%]
BB
Wet
Dry
Transition
(d)
TGM [ng m-3]
1.05
1.00
0.95
0.90
0.85
(e)
CO2 [ppm]
396
395
394
(f)
SIF at 737 nm [mW sr-1 m-2 nm-1]
1.60
1.55
1.50
1.45
1.40
2014-10
2014-11
2014-12
2015-01
2015-02
2015-03
2015-04

633

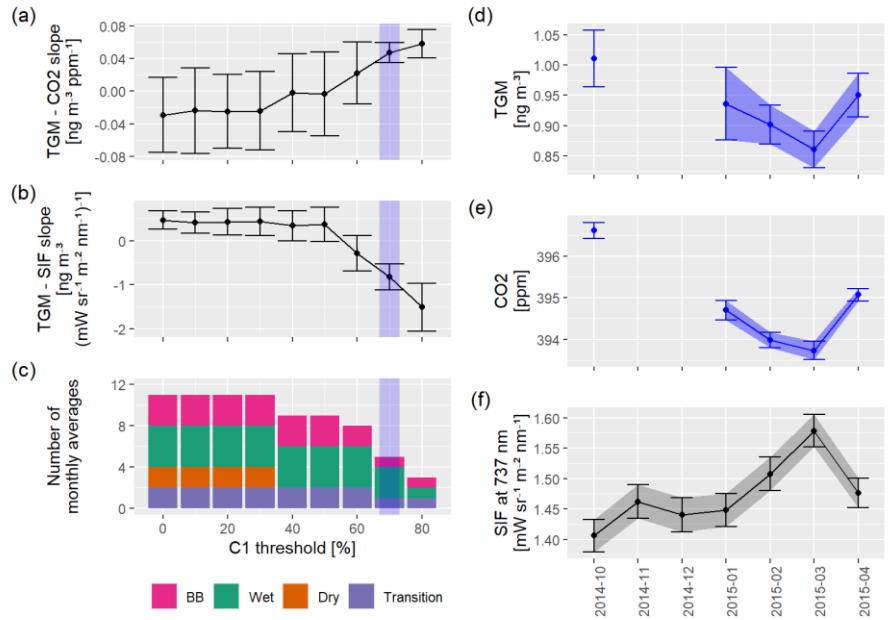
(a)
TGM - CO2 slope [ng m-3 ppm-1]
0.08
0.04
0.00
-0.04
-0.08
(b)
TGM - SIF slope [ng m-3 (mW sr-1 m-2 nm-1)-1]
0
-1
-2
(c)
Number of monthly averages
12
8
4
0
0
20
40
60
80
C1 threshold [%]
BB
Wet
Dry
Transition
(d)
TGM [ng m-3]
1.05
1.00
0.95
0.90
0.85
(e)
CO2 [ppm]
396
395
394
(f)
SIF at 737 nm [mW sr-1 m-2 nm-1]
1.60
1.55
1.50
1.45
1.40
2014-10
2014-11
2014-12
2015-01
2015-02
2015-03
2015-04

634

Fig. 8: Left: Slopes for (a) TGM vs. CO_2 ($TGM = a + b \cdot CO_2$) and (b) TGM vs. SIFTER ($TGM = a + b \cdot SIFTER$) for robust linear models based on monthly averages, as a function of the chosen Amazonian cluster C1 threshold and the resulting selection of data. TGM and CO_2 monthly averages based on less than 30 data points ($n < 30$) were excluded. Error bars show 95% confidence interval. Threshold used for the right-hand side of the plot (C1 mean influence > 70%) shaded in blue. (c) Number of monthly averages available for the linear models at the respective threshold, excluding all monthly averages with $n < 30$. Color shows the partition over the seasons. Right side: Example of the time series of monthly averages for (d) TGM, (e) CO_2, and (f) SIFTER at a C1 selection threshold of 70%. TGM and CO_2 reach their minimum when amazon SIFTER peaks.

Formatted: Font: Italic

These results provide arguments for the presence of a vegetation-related Hg sink in Amazonian air masses, mainly during the wet season. As to be expected from the comparatively low vegetation coverage in the Altiplano, no such correlation with CO_2 or SIFTER was found for air masses of Altiplanic origin. A clear downside to our approach here is that higher selection thresholds for C1, and thus a cleaner selection of northern Amazonian air masses, provide a smaller number of monthly averages available for the linear models (Fig. 8c). Due to the seasonality of transport pathways towards the station (Fig. 5), the available monthly averages of C1 dominated air masses are not equally distributed over the year, but fall mainly into the wet season. As these C1 dominated air masses fall very rarely into the dry season, we cannot make any assumptions about the relationship between TGM and vegetation tracers in lowland air masses during that time of the year.

Concerning our second vegetation proxy, remotely sensed SIFTER averaged over the Amazon rainforest, we have to emphasize the difficulty in linking satellite obtained data with in situ single measurements at CHC, which can only be done under strong assumptions. We chose the whole legal Amazon as a bounding box under the hypothesis that it is, on average, representative of the vegetation that Amazonian C1 dominant air masses are subject to, before arriving at CHC. We further assumed that the average transport time between the Amazon and CHC station is much shorter than one month, so that no lag has to be introduced between monthly averaged satellite and in situ observations (compare to typical transport times shown in Appendix C). Considering these assumptions, our results have to be taken with care, especially as the seasonality of transport pathways does not allow us to discern if the Amazon rainforest would act as a net sink during the entire year, or only as a temporary sink during seasons of high vegetation uptake. Still, the deduced TGM/CO_2 slope at cluster C1 threshold of 80% could be interpreted as our best guess "TGM/CO_2 *uptake ratio*" and be used to constrain the atmospheric mercury uptake by the Amazon rainforest.

4.4 The role of the Pacific Ocean?

Oceanic evasion is a major driver of atmospheric Hg concentrations (Horowitz et al., 2017; Obrist et al., 2018). Especially surface waters of tropical oceans are enriched in mercury, possibly due to enhanced Hg divalent species wet deposition (Horowitz et al., 2017). Soerensen et al. (2014) found anomalously high surface water Hg concentrations and GEM fluxes towards the atmosphere in ocean waters within the Inter-Tropical Convergence Zone (ITCZ). They explained this finding with deep convection and increased Hg divalent species deposition. Floreani et al. (2019~~2018~~) deployed floating flux chambers in the Adriatic Sea and found the highest ocean-atmosphere Hg fluxes in summer, coinciding with increased sea surface temperature (SST) and solar radiation. A

673 similar positive link between SST and atmospheric GEM concentrations was established for Mauna Loa by
674 Carbone et al. (2016).
675 In our dataset, mean TGM concentrations in western-Altiplanic air masses (C5 relative influence > 70%) were
676 significantly higher during the wet season/summer than during the dry season/winter ($0.93 \pm 0.07\, ng\, m^{-3}$ vs.
677 $0.77 \pm 0.01\, ng\, m^{-3}$, $p = 6.65 \cdot 10^{-7}$, Mann-Whitney test), in very good agreement with previous
678 measurements at the Titicaca lake (Guédron et al., 2017). Due to sparse vegetation coverage for cells of that
679 cluster, we can mostly exclude a seasonal influence of vegetation, and anthropogenic influences can be considered
680 unlikely candidates to introduce this sort of seasonal variation considering the low population density and the
681 infrequent use of domestic heating and cooling. To further explore possible causes, we computed the TGM
682 difference between the wet season and the rest of NC as a pollution map and found that air masses originating
683 close to the pacific coast showed much higher TGM concentrations in the wet season (austral summer), compared
684 to the rest of NC (Fig. 9). The opposite was observable for continental air masses, which is likely linked to the
685 possible presence of a vegetation sink effect, as discussed earlier.
686 Thus, we hypothesize that changing emission patterns over the Eastern Pacific Ocean might play a role in the
687 seasonal pattern of atmospheric mercury in the Bolivian Andes. Increased Hg emissions during the wet season
688 (austral summer) might be linked to an increase in SST and/or the southwards shift of the ITCZ and enhanced
689 convection over the southern Pacific Ocean.

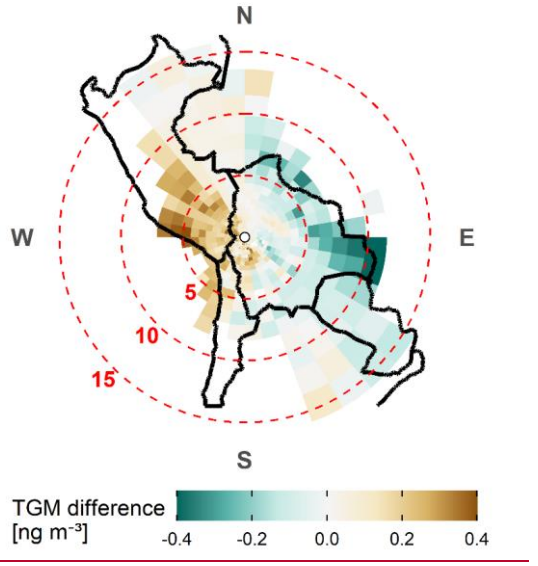

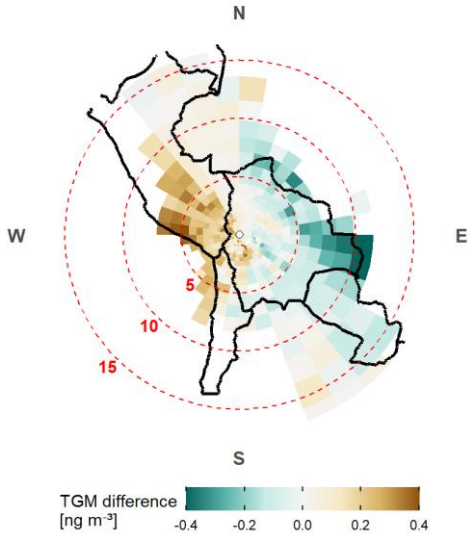

Fig. 9: Pollution map for the wet season (austral summer) minus pollution map for the rest of NC. Polar grid is centered on CHC (white dot). Dashed range circles show the distance ~~Distance~~ to CHC in degrees, convertible to km by using the conversion factor 1° = 108.6 km, with an error below 3% ~~is shown~~ in the whole domain. ~~dashed circles.~~ Trajectory endpoints with an elevation > 1000 m a.g.l. and cells with less than 10 data points (n < 10) were excluded. Color scale capped at the limits.

4.5 Volcanic influences

Previous studies have reported volcanic degassing in the CVZ, both south of CHC (Tamburello et al., 2014; Tassi et al., 2011) and west of CHC (Moussallam et al., 2017). While to our knowledge mercury emissions or atmospheric mercury concentrations have not yet been investigated in the CVZ, a very recent work inferred from mercury concentrations in lichen that volcanoes in the Southern Volcanic Zone (southwards of the CVZ) can be sources of atmospheric mercury (Perez Catán et al., 2020). As similar gas plume compositions (CO_2/S_{TOT}, S_{TOT}/HCl) were measured in volcanic emissions from the CVZ and the Southern Volcanic Zone (Tamburello et al., 2014), we can hypothesize that volcanoes in both active regions also emit mercury in a similar fashion.

That being said, our data gives ambivalent information about the importance of a volcanic Hg source in the region. On one hand, we found elevated mean TGM concentrations of above 1.08 $ng\ m^{-3}$ ($\pm$ 0.08 $ng\ m^{-3}$) in air masses passing at low altitudes (under 1000 m a.g.l) over the south-western frontier between Bolivia and Chile, the same regions of the CVZ where Tassi et al. (2011) and Tamburello et al. (2014) reported important volcanic degassing (Fig. 6a). Southern-Altiplanic cluster C3 in comparison, which represents best the general origin of similar air masses, showed mean TGM concentrations only insignificantly higher than the NC as a whole ($0.92 \pm 0.04\ ng\ m^{-3}$ vs. $0.89 \pm 0.01\ ng\ m^{-3}$, $p = 0.067$, Mann-Whitney test). Admittingly, special care has to be taken with air masses of this general direction, as they move frequently over the urban area of La Paz/El Alto (Chauvigné et al., 2019) before arriving at CHC and could be punctually enriched in Hg, even though the city does overall not seem to play an important role in average Hg concentrations (compare to TGM diel pattern, Fig. 4a). We evaluated this possibility by excluding data with high eBC concentrations (> 87.5th eBC percentile of NC), apparently strongly linked to urban pollution (Fig. 4c, Wiedensohler et al., 2018), without an apparent change in the above results. Therefore, these elevated TGM concentrations in air masses passing over degassing volcanoes to the south of CHC are unlikely caused by urban pollution on the way and might indeed be related to volcanic emissions.

On the other hand, TGM concentrations in air masses passing over the volcanoes Ubinas and Sabancaya to the west of CHC did not appear to be significantly elevated, compared to air masses of similar origin (pollution map, Fig. 6a), even though both volcanoes are currently strongly degassing and account combined for more than half of the entire CVZ volatile fluxes, as estimated by Moussallam et al. (2017). They also lie in a frequent source region for air masses arriving at CHC, especially in the dry season (Fig. 5).

Thus, our data provides an inconclusive picture of the role of the CVZ in the atmospheric mercury budget in the region. While a volcanic mercury source south of CHC can be supported due to significantly elevated TGM concentrations in the source region, we cannot say the same for volcanoes to the west of CHC, even though both Ubinas and Sabancaya were strongly emitting other volcanic gases such as SO_2 during NC (Carn et al., 2017; Moussallam et al., 2017). This inconsistency might be related to the complexity of volcanic mercury emissions, whose quantity is highly variable between different volcanoes, their activity phase, and different points in time (Bagnato et al., 2011; Ferrara et al., 2000). For instance, volcanic Hg/SO_2 emission ratios obtained in literature span several orders of magnitude (Bagnato et al., 2015). Besides, given that our setup does not detect mercury in particulate form, the magnitude of any volcanic signal received at CHC also depends on the mercury gas-particle partitioning at the time of emission, as well as the transformations it undergoes during the transport.

4.6 Artisanal and small scale gold mining (ASGM)

ASGM is known to be a major source of mercury pollution, especially important in Latin America (Esdaile and Chalker, 2018; Obrist et al., 2018). According to recent inventories, South America contributes to 18% of global

Hg emissions to the atmosphere, with 80% of it deriving from the ASGM sector (UNEP GMA 2018). One prominent ASGM hot spot on the continent is the "Madre de Dios" watershed, a few hundred kilometers north of CHC station (Fig. 1), where high Hg concentrations have been found among others in sediments and human hair (Langeland et al., 2017; Martinez et al., 2018).

As shown in Fig. 6b, we measured the highest TGM concentrations in northern Amazonian air masses (cluster C1), which pass mostly over the "Madre de Dios" watershed. Notably, C1 air masses in the wet season showed much higher mean Hg concentrations than the other important lowland cluster C2, which does not pass over this region ($0.91 \pm 0.02\ ng\ m^{-3}$ vs. $0.82 \pm 0.02\ ng\ m^{-3}$, $p = 9.9 \cdot 10^{-12}$, Mann-Whitney test). Still, TGM is uniformly high for most of the north/north-eastern lowland air masses, and the "Madre de Dios" region does not actually appear distinctively in our pollution maps (Fig. 6a). This could be explained by ASGM scattered rather evenly around a large part of the Bolivian lowlands, instead of being clustered around a few hot spots. This is certainly not an unlikely scenario, but it has to be acknowledged that the techniques applied here might not provide the necessary resolution to clearly discern isolated ASGM hotspots hundreds of kilometers away, given dilution and diffusion processes and the uncertainties in HYSPLIT trajectories.

5. Conclusions

Our measurements of TGM at the mountain site CHC fill an important gap in observations for South America and allow us to make justified assumptions about the dynamics of atmospheric mercury on the continent.

During NC, mean TGM concentrations at CHC were relatively low compared to other sites in the Southern Hemisphere, but similar to those in South America. However, we detected a significant rise of atmospheric Hg levels during EC, which might well be related to the 2015 – 2016 "El Niño", a hypothesis we will address in an upcoming publication. In the regional overview, mercury concentrations were higher in air masses with northern Amazonian or southern Altiplanic origin, the former possibly related to a strong ASGM presence in the source region, while the latter might be of volcanic origin. In agreement with other South American sites, but in contrast to different regions in the Southern Hemisphere, we observed a marked seasonal pattern. Concentrations were lowest in the dry season (austral winter), rising in the BB season, and highest in the beginning of the wet season (austral summer). To explain this, we explored several possible drivers for this seasonal cycle. Biomass burning related Hg emissions appear to significantly raise atmospheric Hg levels during a limited time of the year, mainly between August and October (BB season). Vegetation on the continent, most prominently the Amazon rainforest, seems to act as an important mercury sink, at least during months of high gross primary production (around February – April). The former allowed us to deduce a TGM/CO emission ratio of $(2.3 \pm 0.6) \cdot 10^{-7} ppbv_{TGM}\ ppbv_{CO}{}^{-1}$, while we used the latter to infer a "best guess" TGM/CO_2 *uptake ratio* of $0.058 \pm$

772 $0.017\ (ng\ m^{-3})_{TGM}\ ppm_{CO2}{}^{-1}$. Finally, arguments can be made for a significant influence of the Eastern Pacific
773 Ocean on regional Hg levels, possibly through a shift in ocean-atmosphere Hg exchanges in response to rising sea
774 surface temperature and deep convection in austral summer.

775 Notably, all three of these major regional drivers of atmospheric mercury might undergo significant changes in
776 the near future. On one hand, Pacific SST and convection dynamics could shift as a consequence of climate
777 change. On the other hand, both upcoming BB emissions and the magnitude of the South American vegetation
778 sink will depend heavily on the future of the Amazon rainforest, which itself is threatened by climate change and
779 changes in land-use, e.g., deforestation and agricultural practices. In perspective, the TGM/CO emission ratio and
780 TGM/CO_2 *uptake ratio* obtained here could be used to constrain both current and future South American biomass
781 burning Hg emissions and vegetation Hg uptake, with the help of remotely sensed CO and CO_2 data products and
782 model results.

783
784

Appendix A: Seasonality of CO concentrations in South America and CHC

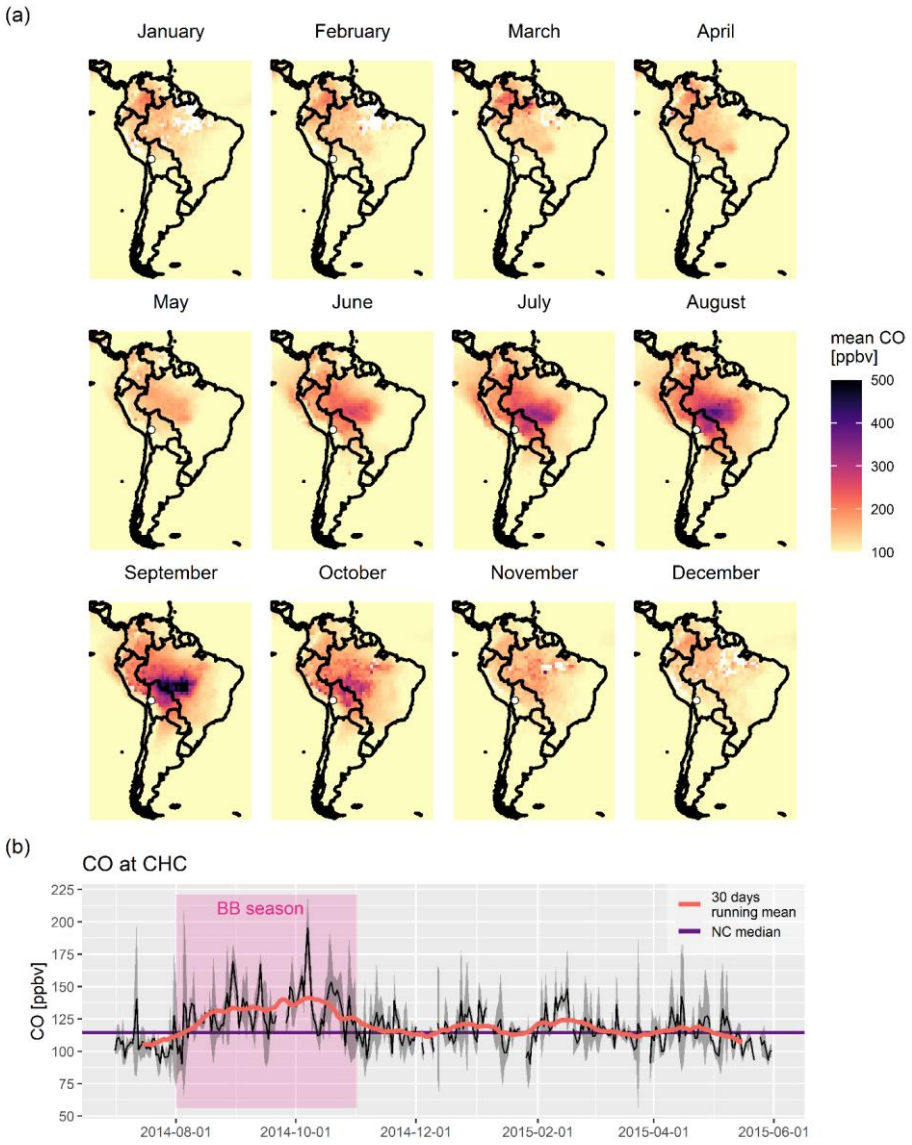
(a)
January
February
March
April
May
June
July
August
September
October
November
December
mean CO [ppbv]
500
400
300
200
100
(b)
CO at CHC
BB season
30 days running mean
NC median
CO [ppbv]
225
200
175
150
125
100
75
50
2014-08-01
2014-10-01
2014-12-01
2015-02-01
2015-04-01
2015-06-01

786

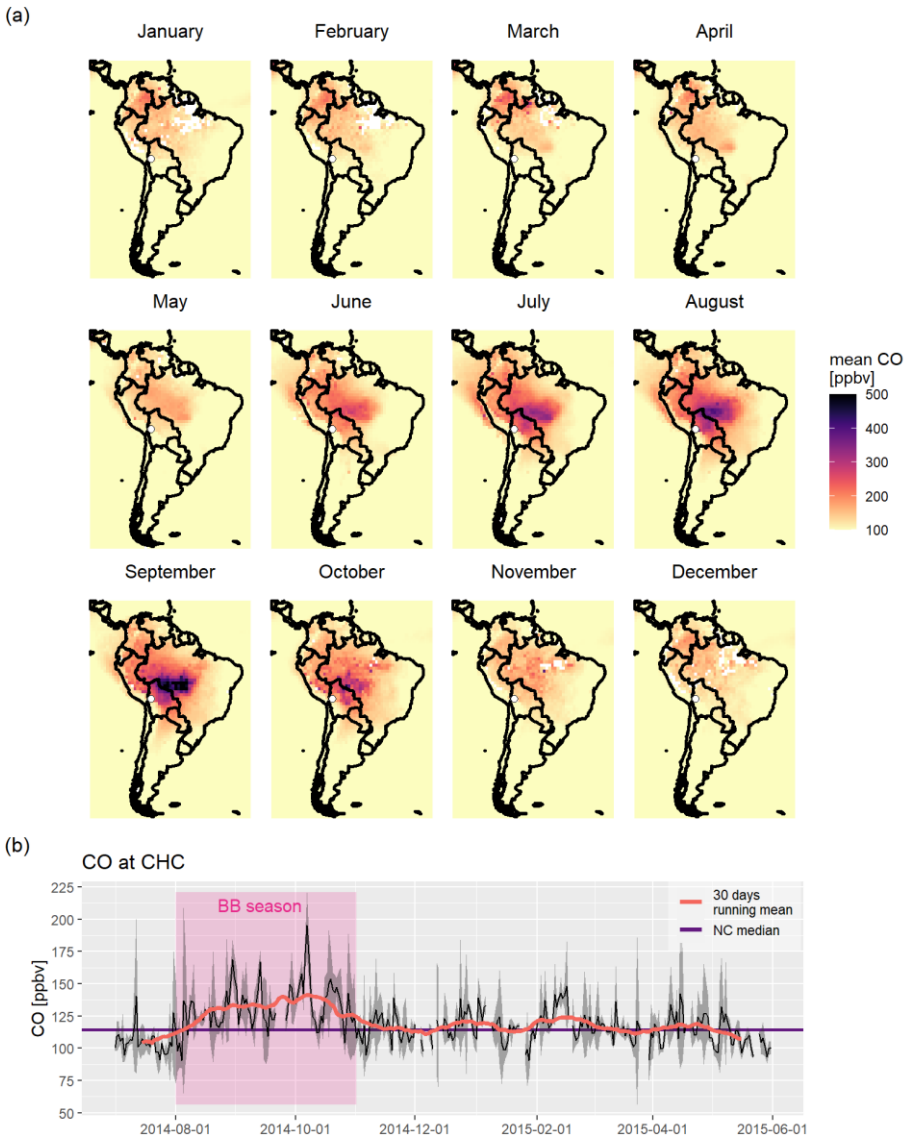

Fig. A1. (a) Seasonality of remotely sensed tropospheric CO concentrations in South America, from 01.2005 to 01.2015 and based on the MOP03J_V008 data product (Ziskin, 2019). The white dot shows the CHC station. (b) Daily mean CO concentrations at CHC during "normal conditions" (NC: 2014-07-01 until 2015-06-01). Grey shaded area shows the standard deviation, orange line the 30 days running mean, purple line the NC median. The pink box illustrates the definition of the biomass burning (BB) season used in the present work.

Appendix B: Pollution maps at different cutoff altitudes

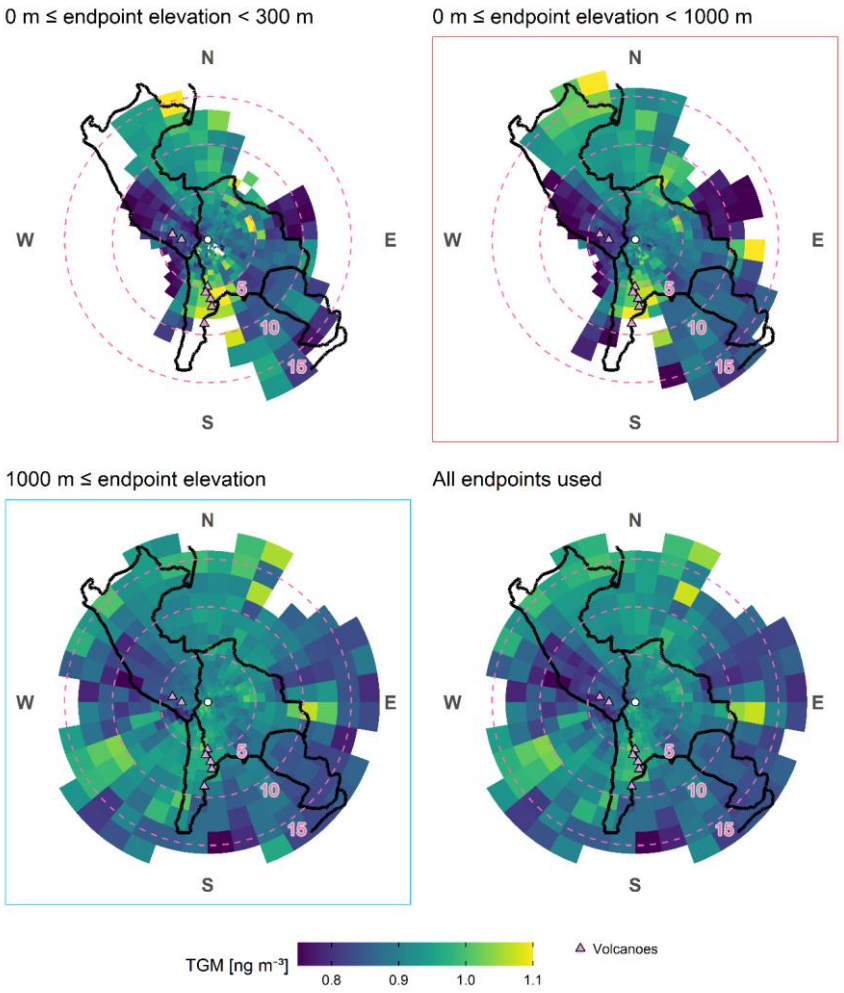
0 m ≤ endpoint elevation < 300 m
0 m ≤ endpoint elevation < 1000 m
1000 m ≤ endpoint elevation
All endpoints used
N
W
E
S
5
10
15
TGM [ng m⁻³]
0.8
0.9
1.0
1.1
Volcanoes

794

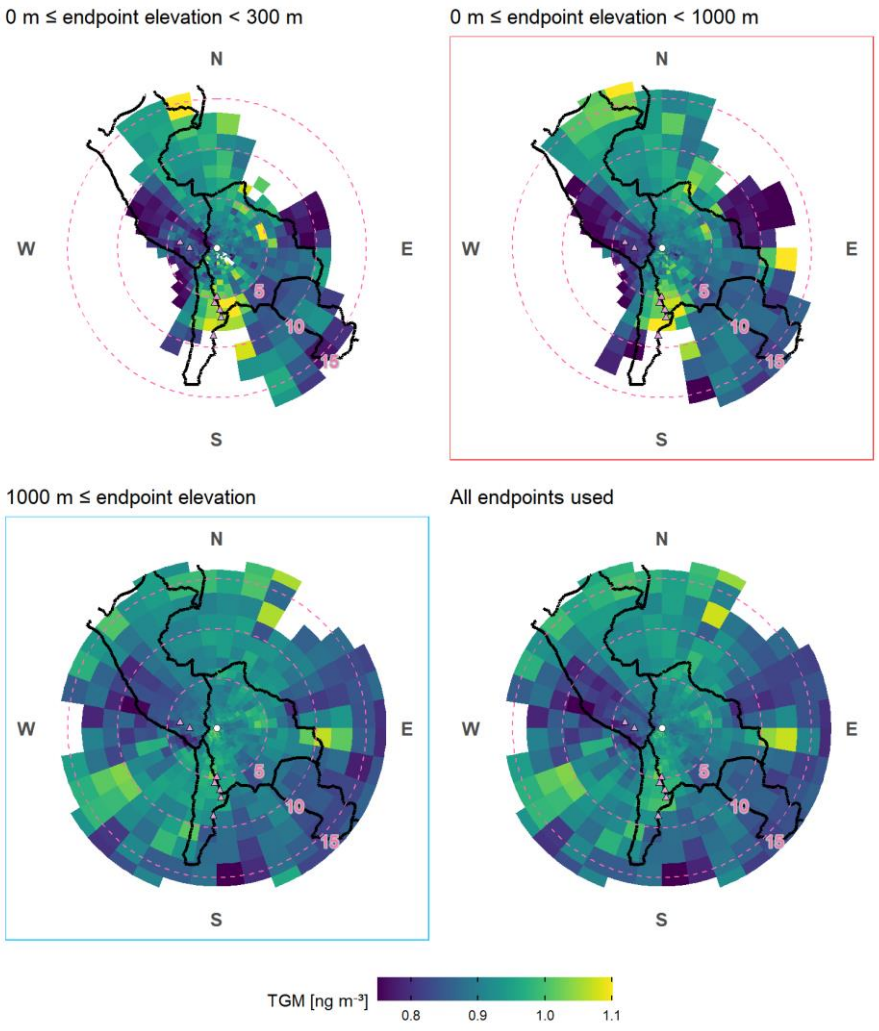

Fig. B1: Pollution maps~~Pollutions map~~ based on all TGM data taken during NC, calculated by using different cutoff altitudes as specified by the plot title. The plot corresponding to the cutoff – altitude used in the main text (endpoint elevation < 1000 m a.g.l) is framed in red. The plot based on all endpoints which were excluded from the pollution map shown in the main text is framed in blue. Dashed range circles show the distance to CHC in degrees, convertible to km by using the conversion factor 1° = 108.6 km, with an error below 3% in the whole domain.~~.~~ Color scale capped at the limits. Cells with less than 10 data points (n < 10) were excluded. Pink triangles show selected degassing volcanoes in the CVZ, from north to south: Sabancaya, Ubinas, Ollague, San Pedro, Putana, Lascar, Lastarria.

Appendix C: Median transport time for HYSPLIT back-trajectories arriving at CHC

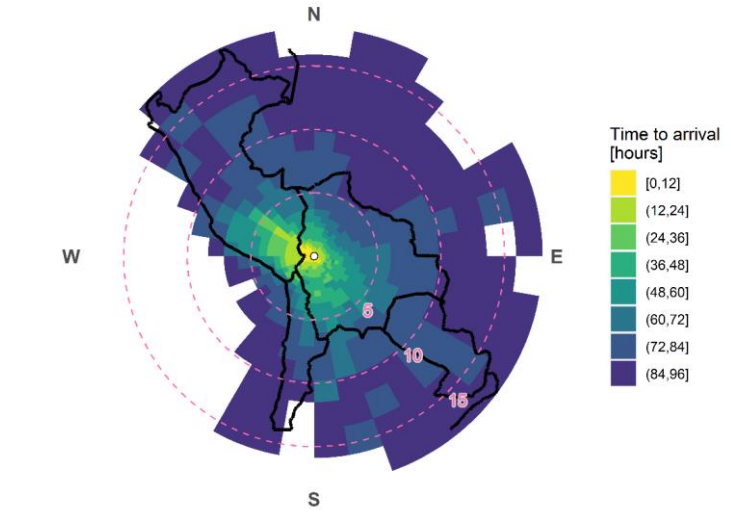

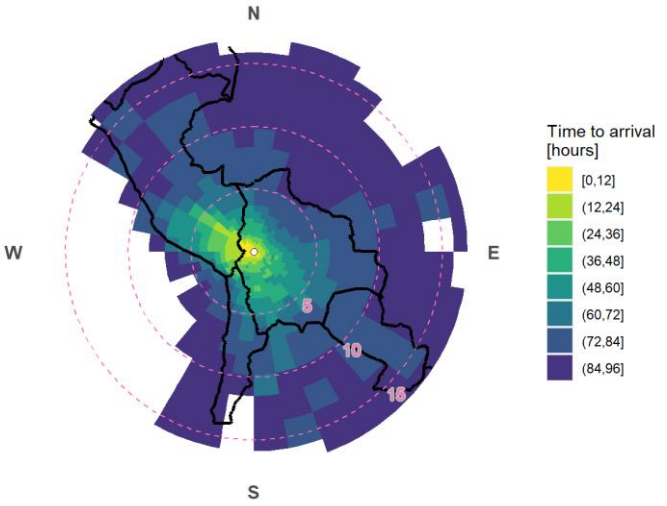

Fig. C1: Average transport time between air mass source region and CHC, shown through the median time passed between HYSPLIT trajectory pixel piercing and arrival at CHC. Dashed range circles show the distance ~~Distance~~ to CHC ~~(white dot)~~ in degrees, convertible to km by using the conversion factor 1° = 108.6 km, with an error below 3% ~~is shown~~ in the whole domain. ~~dashed range circles.~~ Based on all trajectories during NC (01.07.2014 - 01.06.2015) and endpoints with an elevation below 1000 m a.g.l.

Formatted: Font: 11 pt, Not Italic

814
815
816
817

Appendix D: Sensitivity analysis for the calculation of the TGM/CO emission ratio

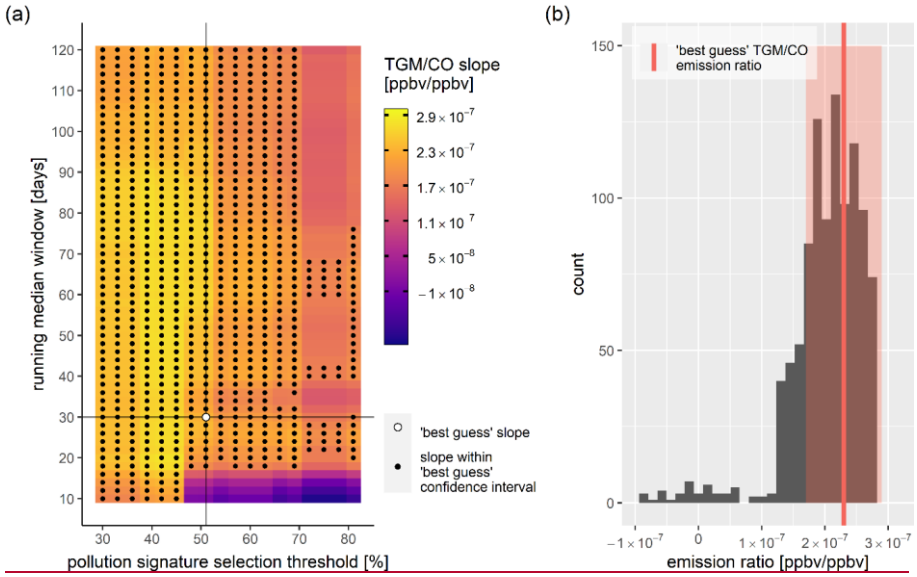

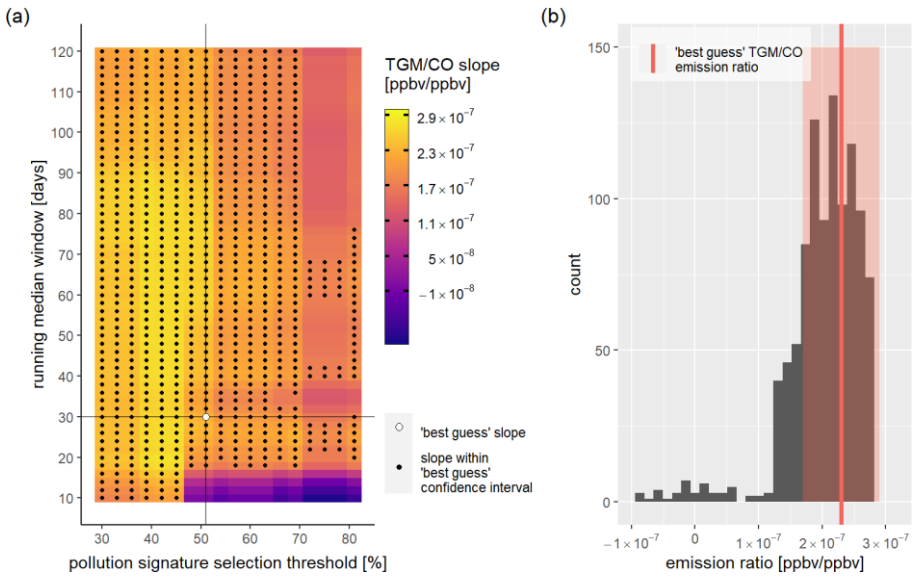

Fig. D1: Sensitivity analysis for the calculation of the TGM/CO emission ratio as a function of the chosen threshold for the selection of biomass burning pollution signatures (percentage of time the pollution signature fell into the BB season) and the choice on the size of the "running window" (in days) to calculate the median TGM background concentrations. (a) Heatmap showing the obtained TGM/CO emission ratios for a wide range of combinations of the pollution signature threshold (x-axis) and the running window (y-axis). "Best guess"

826 *TGM/CO emission ratio as presented in the main text marked as white dot, black dots show all combinations for*
827 *which the calculated slope is within the "best guess" confidence interval. (b) Histogram for all TGM/CO slopes*
828 *shown in (a) (the heatmap). "Best guess" emission ratio and its confidence interval in red.*

829

Data availability:

Chacaltaya L1 TGM data are freely available at https://gmos.aeris-data.fr/.

BC lev2 can be found at http://ebas.nilu.no/

CO2 is provided by the French monitoring network SNO-ICOS-France-Atmosphere

SIFTER data as described in Koren et al. (2018) can be found under: https://doi.org/10.18160/ECK0-1Y4C

MOPITT CO gridded daily averages (Near and Thermal Infrared Radiances) were obtained from the NASA Langley Research Center Atmospheric Science Data Center.

Competing interests:

The authors declare that they have no conflict of interest.

Autor contribution:

Alkuin Maximilian Koenig performed data analysis, prepared figures, and prepared the manuscript. Olivier Magand collected TGM data, was part in scientific discussions, data interpretation, and the manuscript preparation. Paolo Laj was part in scientific discussions and the manuscript preparation. Marcos Andrade provided data, was part in scientific discussions, and the manuscript preparation. Isabel Moreno collected data, was part in scientific discussions, and the manuscript preparation. Fernando Velarde collected data, was part in scientific discussions, and the manuscript preparation. Grover Salvatierra collected data and performed data analysis. René Gutierrez was part in data collection and scientific discussions. Luis Blacutt was part in scientific discussions, and the manuscript preparation. Diego Aliaga performed data analysis, was part in scientific discussions, and the manuscript preparation. Thomas Reichler was part in computation, scientific discussions, and the manuscript preparation. Karine Sellegri provided data, was part in scientific discussions and the manuscript preparation, Olivier Laurent collected data. Michel Ramonet provided data, was part in scientific discussions and the manuscript preparation, Aurélien Dommergue designed the experiment, collected data, was part in scientific discussions, and the manuscript preparation.

Acknowledgments

This research paper is part of the GMOS-Train project that has received funding from the European Union's Horizon 2020 research and innovation programme under the Marie Skłodowska-Curie grant agreement No. 860497. These observations contribute to the GEO GOS4M (Global Observation System for Mercury

Field Code Changed

Field Code Changed

Field Code Changed

Field Code Changed

(www.gos4m.org). It is aimed to support the UN Global Partnership on Mercury Fate and Transport Research (UN F&T) of the UN environment in the implementation of the Minamata Convention (www.mercuryconvention.org) by providing a Knowledge Platform on mercury in the environment and human health. It will support UN environment and Nations to assess the effectiveness of measures that will be undertaken. CHC TGM data accessible in GMOS-FR have been collected through funding obtained by the European Union 7th Framework Programme project Global Mercury Observation System (GMOS 2010-2015), LabEX OSUG@2020 (ANR10 LABX56), LEFE CNRS/INSU (SAMOA program), SNO CLAP and also by ACTRIS-France National Research infrastructure. We also acknowledge the logistical and financial support from IRD (Institut de Recherche pour le Développement) and LFA during the field campaign in Bolivia. CO_2 observations are obtained as part of the French monitoring network SNO-IFA. We acknowledge the financial support provided by the mobility project PAPILA (Prediction of Air Pollution in Latin America and the Caribbean). Analyses and visualizations used in this study were produced with the Giovanni online data system, developed and maintained by the NASA GES DISC.

Field Code Changed

References

Ambrizzi, T., de Souza, E. B. and Pulwarty, R. S.: The Hadley and Walker Regional Circulations and Associated ENSO Impacts on South American Seasonal Rainfall, in The Hadley Circulation: Present, Past and Future, vol. 21, edited by H. F. Diaz and R. S. Bradley, pp. 203–235, Springer Netherlands, Dordrecht., 2004.

Ambrose, J. L.: Improved methods for signal processing in measurements of mercury by Tekran® 2537A and 2537B instruments, Atmos. Meas. Tech., 10(12), 5063–5073, https://doi.org/10.5194/amt-10-5063-2017, 2017.

Andrade, M., Zaratti, F., Forno, R., Gutiérrez, R., Moreno, I., Velarde, F., Ávila, F., Roca, M., Sánchez, M. F., Laj, P., Jaffrezo, J. L., Ginot, P., Sellegri, K., Ramonet, M., Laurent, O., Weinhold, K., Wiedensohler, A., Krejci, R., Bonasoni, P., Cristofanelli, P., Whiteman, D., Vimeux, F., Dommergue, A., Magand, O. and M. Andrade: Puesta en marcha de una nueva estación de monitoreo climático en los andes centrales de Bolivia: la estación Gaw/Chacaltaya, Revista Boliviana de Física, 26, 6–15, 2015.

Angot, H., Barret, M., Magand, O., Ramonet, M. and Dommergue, A.: A 2-year record of atmospheric mercury species at a background Southern Hemisphere station on Amsterdam Island, Atmos. Chem. Phys., 14(20), 11461–11473, doi:10.5194/acp-14-11461-2014, 2014.

Bagnato, E., Aiuppa, A., Parello, F., Allard, P., Shinohara, H., Liuzzo, M. and Giudice, G.: New clues on the contribution of Earth's volcanism to the global mercury cycle, Bull Volcanol, 73(5), 497–510, https://doi.org/10.1007/s00445-010-0419-y, 2011.

Bagnato, E., Tamburello, G., Avard, G., Martinez-Cruz, M., Enrico, M., Fu, X., Sprovieri, M. and Sonke, J. E.: Mercury fluxes from volcanic and geothermal sources: an update, Geological Society, London, Special Publications, 410(1), 263–285, https://doi.org/10.1144/SP410.2, 2015.

Beal, S. A., Jackson, B. P., Kelly, M. A., Stroup, J. S. and Landis, J. D.: Effects of Historical and Modern Mining on Mercury Deposition in Southeastern Peru, Environ. Sci. Technol., 47(22), 12715–12720, https://doi.org/10.1021/es402317x, 2013.

Beal, S. A., Kelly, M. A., Stroup, J. S., Jackson, B. P., Lowell, T. V. and Tapia, P. M.: Natural and anthropogenic variations in atmospheric mercury deposition during the Holocene near Quelccaya Ice Cap, Peru: Holocene Mercury Deposition, Global Biogeochem. Cycles, 28(4), 437–450, https://doi.org/10.1002/2013GB004780, 2014.

Bloom, N. and Fitzgerald, W. F.: Determination of volatile mercury species at the picogram level by low-temperature gas chromatography with cold-vapour atomic fluorescence detection, Analytica Chimica Acta, 208, 151–161, doi:10.1016/S0003-2670(00)80743-6, 1988.

Bond, T. C. and Bergstrom, R. W.: Light Absorption by Carbonaceous Particles: An Investigative Review, Aerosol Science and Technology, 40(1), 27–67, doi:10.1080/02786820500421521, 2006.

Cape, J. N., Coyle, M. and Dumitrean, P.: The atmospheric lifetime of black carbon, Atmospheric Environment, 59, 256–263, doi:10.1016/j.atmosenv.2012.05.030, 2012.

Carbone, F., Landis, M. S., Gencarelli, C. N., Naccarato, A., Sprovieri, F., De Simone, F., Hedgecock, I. M. and Pirrone, N.: Sea surface temperature variation linked to elemental mercury concentrations measured on Mauna

910 Loa: SST AND HG(0) CONCENTRATION ON MAUNA LOA, Geophys. Res. Lett., 43(14), 7751–7757,
911 doi:10.1002/2016GL069252, 2016.

912 Carn, S. A., Fioletov, V. E., McLinden, C. A., Li, C. and Krotkov, N. A.: A decade of global volcanic SO2
913 emissions measured from space, Sci Rep, 7(1), 44095, doi:10.1038/srep44095, 2017.

914 Chauvigné, A., Aliaga, D., Sellegri, K., Montoux, N., Krejci, R., Močnik, G., Moreno, I., Müller, T., Pandolfi,
915 M., Velarde, F., Weinhold, K., Ginot, P., Wiedensohler, A., Andrade, M. and Laj, P.: Biomass burning and
916 urban emission impacts in the Andes Cordillera region based on in situ measurements from the Chacaltaya
917 observatory, Bolivia (5240 m a.s.l.), Atmos. Chem. Phys., 19(23), 14805–14824,
918 doi:10.5194/acp-19-14805-2019, 2019.

919 Choi, Y., Kanaya, Y., Park, S.-M., Matsuki, A., Sadanaga, Y., Kim, S.-W., Uno, I., Pan, X., Lee, M., Kim, H.
920 and Jung, D. H.: Regional variability in black carbon and carbon monoxide ratio from long-term observations
921 over East Asia: assessment of representativeness for black carbon (BC) and carbon monoxide (CO) emission
922 inventories, Atmos. Chem. Phys., 20(1), 83–98, doi:10.5194/acp-20-83-2020, 2020.

923 D'Amore, F., Bencardino, M., Cinnirella, S., Sprovieri, F. and Pirrone, N.: Data quality through a web-based
924 QA/QC system: implementation for atmospheric mercury data from the global mercury observation system,
925 Environ. Sci.: Processes Impacts, 17(8), 1482–1491, doi:10.1039/C5EM00205B, 2015.

926 Diéguez, M. C., Bencardino, M., García, P. E., D'Amore, F., Castagna, J., De Simone, F., Soto Cárdenas, C.,
927 Ribeiro Guevara, S., Pirrone, N. and Sprovieri, F.: A multi-year record of atmospheric mercury species at a
928 background mountain station in Andean Patagonia (Argentina): Temporal trends and meteorological influence,
929 Atmospheric Environment, 214, 116819, doi:10.1016/j.atmosenv.2019.116819, 2019.

930 Diringer, S. E., Feingold, B. J., Ortiz, E. J., Gallis, J. A., Araújo-Flores, J. M., Berky, A., Pan, W. K. Y. and
931 Hsu-Kim, H.: River transport of mercury from artisanal and small-scale gold mining and risks for dietary
932 mercury exposure in Madre de Dios, Peru, Environ. Sci.: Processes Impacts, 17(2), 478–487,
933 doi:10.1039/C4EM00567H, 2015.

934 Diringer, S. E., Berky, A. J., Marani, M., Ortiz, E. J., Karatum, O., Plata, D. L., Pan, W. K. and Hsu-Kim, H.:
935 Deforestation Due to Artisanal and Small-Scale Gold Mining Exacerbates Soil and Mercury Mobilization in
936 Madre de Dios, Peru, Environ. Sci. Technol., acs.est.9b06620, doi:10.1021/acs.est.9b06620, 2019.

937 Dumarey, R., Temmerman, E., Adams, R. and Hoste, J.: The accuracy of the vapour-injection calibration
938 method for the determination of mercury by amalgamation/cold-vapour atomic absorption spectrometry,
939 Analytica Chimica Acta, 170, 337–340, doi:10.1016/S0003-2670(00)81759-6, 1985.

940 Ebinghaus, R., Slemr, F., Brenninkmeijer, C. A. M., van Velthoven, P., Zahn, A., Hermann, M., O'Sullivan, D.
941 A. and Oram, D. E.: Emissions of gaseous mercury from biomass burning in South America in 2005 observed
942 during CARIBIC flights: HG EMISSION FROM BIOMASS BURNING, Geophys. Res. Lett., 34(8),
943 doi:10.1029/2006GL028866, 2007.

944 Erfanian, A., Wang, G. and Fomenko, L.: Unprecedented drought over tropical South America in 2016:
945 significantly under-predicted by tropical SST, Sci Rep, 7(1), 5811, doi:10.1038/s41598-017-05373-2, 2017.

946 Ericksen, J. A., Gustin, M. S., Schorran, D. E., Johnson, D. W., Lindberg, S. E. and Coleman, J. S.:
947 Accumulation of atmospheric mercury in forest foliage, Atmospheric Environment, 37(12), 1613–1622,
948 doi:10.1016/S1352-2310(03)00008-6, 2003.

949 Esdaile, L. J. and Chalker, J. M.: The Mercury Problem in Artisanal and Small-Scale Gold Mining, Chem. Eur.
950 J., 24(27), 6905–6916, doi:10.1002/chem.201704840, 2018.

951 Figueiredo, B. R., De Campos, A. B., Da Silva, R. and Hoffman, N. C.: Mercury sink in Amazon rainforest: soil
952 geochemical data from the Tapajos National Forest, Brazil, Environ Earth Sci, 77(8), 296, doi:10.1007/s12665-
953 018-7471-x, 2018.

954 Fitzgerald, W. F. and Gill, G. A.: Subnanogram determination of mercury by two-stage gold amalgamation and
955 gas phase detection applied to atmospheric analysis, Anal. Chem., 51(11), 1714–1720,
956 doi:10.1021/ac50047a030, 1979.

957 Floreani, F., Acquavita, A., Petranich, E. and Covelli, S.: Diurnal fluxes of gaseous elemental mercury from the
958 water-air interface in coastal environments of the northern Adriatic Sea, Science of The Total Environment, 668,
959 925–935, https://doi.org/10.1016/j.scitotenv.2019.03.012, 2019.

960 Fostier, A. H., Melendez-Perez, J. J. and Richter, L.: Litter mercury deposition in the Amazonian rainforest,
961 Environmental Pollution, 206, 605–610, doi:10.1016/j.envpol.2015.08.010, 2015.

962 Frankenberg, C., Fisher, J. B., Worden, J., Badgley, G., Saatchi, S. S., Lee, J.-E., Toon, G. C., Butz, A., Jung,
963 M., Kuze, A. and Yokota, T.: New global observations of the terrestrial carbon cycle from GOSAT: Patterns of
964 plant fluorescence with gross primary productivity: CHLOROPHYLL FLUORESCENCE FROM SPACE,
965 Geophys. Res. Lett., 38(17), n/a-n/a, doi:10.1029/2011GL048738, 2011.

966 Fraser, A., Dastoor, A. and Ryjkov, A.: How important is biomass burning in Canada to mercury
967 contamination?, Atmos. Chem. Phys., 18(10), 7263–7286, doi:10.5194/acp-18-7263-2018, 2018.

968 Friedli, H. R., Arellano, A. F., Cinnirella, S. and Pirrone, N.: Initial Estimates of Mercury Emissions to the
969 Atmosphere from Global Biomass Burning, Environ. Sci. Technol., 43(10), 3507–3513,
970 https://doi.org/10.1021/es802703g, 2009.

971 Graciela, A., Maria, K. and de Freitas, S. R.: Biomass Burning in South America: Transport Patterns and
972 Impacts, in Biomass - Detection, Production and Usage, edited by M. D. Matovic, InTech., 2011.

973 Grigal, D. F.: Mercury Sequestration in Forests and Peatlands: A Review, J. Environ. Qual., 32(2), 393–405,
974 doi:10.2134/jeq2003.3930, 2003.

975 Guédron, S., Point, D., Acha, D., Bouchet, S., Baya, P. A., Tessier, E., Monperrus, M., Molina, C. I., Groleau,
976 A., Chauvaud, L., Thebault, J., Amice, E., Alanoca, L., Duwig, C., Uzu, G., Lazzaro, X., Bertrand, A., Bertrand,
977 S., Barbraud, C., Delord, K., Gibon, F. M., Ibanez, C., Flores, M., Fernandez Saavedra, P., Ezpinoza, M. E.,
978 Heredia, C., Rocha, F., Zepita, C. and Amouroux, D.: Mercury contamination level and speciation inventory in
979 Lakes Titicaca & Uru-Uru (Bolivia): Current status and future trends, Environmental Pollution, 231, 262–270,
980 doi:10.1016/j.envpol.2017.08.009, 2017.

Horowitz, H. M., Jacob, D. J., Zhang, Y., Dibble, T. S., Slemr, F., Amos, H. M., Schmidt, J. A., Corbitt, E. S., Marais, E. A. and Sunderland, E. M.: A new mechanism for atmospheric mercury redox chemistry: implications for the global mercury budget, Atmos. Chem. Phys., 17(10), 6353–6371, doi:10.5194/acp-17-6353-2017, 2017.

~~Howard, D., Nelson, P. F., Edwards, G. C., Morrison, A. L., Fisher, J. A., Ward, J., Harnwell, J., van der Schoot, M., Atkinson, B., Chambers, S. D., Griffiths, A. D., Werczynski, S. and Williams, A. G.: Atmospheric mercury in the southern hemisphere tropics: seasonal and diurnal variations and influence of inter-hemispheric transport, preprint, Gases/Field Measurements/Troposphere/Chemistry (chemical composition and reactions), 2017a.~~

Howard, D., Nelson, P. F., Edwards, G. C., Morrison, A. L., Fisher, J. A., Ward, J., Harnwell, J., van der Schoot, M., Atkinson, B., Chambers, S. D., Griffiths, A. D., Werczynski, S. and Williams, A. G.: Atmospheric mercury in the Southern Hemisphere tropics: seasonal and diurnal variations and influence of inter-hemispheric transport, Atmos. Chem. Phys., 17(18), 11623–11636, https://doi.org/:10.5194/acp-17-11623-2017, 2017~~2017b~~.

Jiskra, M., Wiederhold, J. G., Skyllberg, U., Kronberg, R.-M., Hajdas, I. and Kretzschmar, R.: Mercury Deposition and Re-emission Pathways in Boreal Forest Soils Investigated with Hg Isotope Signatures, Environ. Sci. Technol., 49(12), 7188–7196, doi:10.1021/acs.est.5b00742, 2015.

Jiskra, M., Sonke, J. E., Obrist, D., Bieser, J., Ebinghaus, R., Myhre, C. L., Pfaffhuber, K. A., Wängberg, I., Kyllönen, K., Worthy, D., Martin, L. G., Labuschagne, C., Mkololo, T., Ramonet, M., Magand, O. and Dommergue, A.: A vegetation control on seasonal variations in global atmospheric mercury concentrations, Nature Geosci, 11(4), 244–250, doi:10.1038/s41561-018-0078-8, 2018.

Khalil, M. A. K. and Rasmussen, R. A.: The global cycle of carbon monoxide: Trends and mass balance, Chemosphere, 20(1–2), 227–242, doi:10.1016/0045-6535(90)90098-E, 1990.

Kooreman, M. L., Boersma, K. F., van Schaik, E., van Versendaal, R., Cacciari, A. and Tuinder, O. N. E.: SIFTER sun-induced vegetation fluorescence data from GOME-2A (Version 2.0), , doi:10.21944/GOME2A-SIFTER-V2-SUN-INDUCED-FLUORESCENCE, 2020.

Koren, G., van Schaik, E., Araújo, A. C., Boersma, K. F., Gärtner, A., Killaars, L., Kooreman, M. L., Kruijt, B., van der Laan-Luijkx, I. T., von Randow, C., Smith, N. E. and Peters, W.: Widespread reduction in sun-induced fluorescence from the Amazon during the 2015/2016 El Niño, Phil. Trans. R. Soc. B, 373(1760), 20170408, doi:10.1098/rstb.2017.0408, 2018.

Lamborg, C. H., Hammerschmidt, C. R., Bowman, K. L., Swarr, G. J., Munson, K. M., Ohnemus, D. C., Lam, P. J., Heimbürger, L.-E., Rijkenberg, M. J. A. and Saito, M. A.: A global ocean inventory of anthropogenic mercury based on water column measurements, Nature, 512(7512), 65–68, https://doi.org/10.1038/nature13563, 2014.

Langeland, A., Hardin, R. and Neitzel, R.: Mercury Levels in Human Hair and Farmed Fish near Artisanal and Small-Scale Gold Mining Communities in the Madre de Dios River Basin, Peru, IJERPH, 14(3), 302, doi:10.3390/ijerph14030302, 2017.

~~Leduc, G., Vidal, L., Tachikawa, K., Rostek, F., Sonzogni, C., Beaufort, L. and Bard, E.: Moisture transport across Central America as a positive feedback on abrupt climatic changes, Nature, 445(7130), 908–911, doi:10.1038/nature05578, 2007.~~

Luus, K. A., Commane, R., Parazoo, N. C., Benmergui, J., Euskirchen, E. S., Frankenberg, C., Joiner, J., Lindaas, J., Miller, C. E., Oechel, W. C., Zona, D., Wofsy, S. and Lin, J. C.: Tundra photosynthesis captured by satellite-observed solar-induced chlorophyll fluorescence, Geophys. Res. Lett., 44(3), 1564–1573, doi:10.1002/2016GL070842, 2017.

Martin, L. G., Labuschagne, C., Brunke, E.-G., Weigelt, A., Ebinghaus, R. and Slemr, F.: Trend of atmospheric mercury concentrations at Cape Point for 1995–2004 and since 2007, Atmos. Chem. Phys., 17(3), 2393–2399, doi:10.5194/acp-17-2393-2017, 2017.

Martinez, G., McCord, S., Driscoll, C., Todorova, S., Wu, S., Araújo, J., Vega, C. and Fernandez, L.: Mercury Contamination in Riverine Sediments and Fish Associated with Artisanal and Small-Scale Gold Mining in Madre de Dios, Peru, IJERPH, 15(8), 1584, https://doi.org/10.3390/ijerph15081584, 2018.

McGill, R., Tukey, J. W. and Larsen, W. A.: Variations of Box Plots, The American Statistician, 32(1), 12, https://doi.org/10.2307/2683468, 1978.

Michelazzo, P. A. M., Fostier, A. H., Magarelli, G., Santos, J. C. and de Carvalho, J. A.: Mercury emissions from forest burning in southern Amazon: MERCURY EMISSIONS FROM FOREST BURNING, Geophys. Res. Lett., 37(9), n/a-n/a, doi:10.1029/2009GL042220, 2010.

Morgan, W. T., Darbyshire, E., Spracklen, D. V., Artaxo, P. and Coe, H.: Non-deforestation drivers of fires are increasingly important sources of aerosol and carbon dioxide emissions across Amazonia, Sci Rep, 9(1), 16975, doi:10.1038/s41598-019-53112-6, 2019.

Moussallam, Y., Tamburello, G., Peters, N., Apaza, F., Schipper, C. I., Curtis, A., Aiuppa, A., Masias, P., Boichu, M., Bauduin, S., Barnie, T., Bani, P., Giudice, G. and Moussallam, M.: Volcanic gas emissions and degassing dynamics at Ubinas and Sabancaya volcanoes; implications for the volatile budget of the central volcanic zone, Journal of Volcanology and Geothermal Research, 343, 181–191, doi:10.1016/j.jvolgeores.2017.06.027, 2017.

Munthe, J., Sprovieri, F., Horvat, M., and Ebinghaus, R.: SOPs and QA/QC protocols regarding measurements of TGM, GEM, RGM, TPM and mercury in precipitation in cooperation with WP3, WP4, and WP5, GMOS deliverable 6.1, CNR-IIA, IVL, available at http://www.gmos.eu (last access on), 2011.

Müller, D., Wip, D., Warneke, T., Holmes, C. D., Dastoor, A. and Notholt, J.: Sources of atmospheric mercury in the tropics: continuous observations at a coastal site in Suriname, Atmos. Chem. Phys., 12(16), 7391–7397, doi:10.5194/acp-12-7391-2012, 2012.

Müller, T., Henzing, J. S., de Leeuw, G., Wiedensohler, A., Alastuey, A., Angelov, H., Bizjak, M., Collaud Coen, M., Engström, J. E., Gruening, C., Hillamo, R., Hoffer, A., Imre, K., Ivanow, P., Jennings, G., Sun, J. Y., Kalivitis, N., Karlsson, H., Komppula, M., Laj, P., Li, S.-M., Lunder, C., Marinoni, A., Martins dos Santos, S., Moerman, M., Nowak, A., Ogren, J. A., Petzold, A., Pichon, J. M., Rodriquez, S., Sharma, S., Sheridan, P. J.,

Teinilä, K., Tuch, T., Viana, M., Virkkula, A., Weingartner, E., Wilhelm, R. and Wang, Y. Q.: Characterization and intercomparison of aerosol absorption photometers: result of two intercomparison workshops, Atmos. Meas. Tech., 4(2), 245–268, doi:10.5194/amt-4-245-2011, 2011.

Obrist, D.: Atmospheric mercury pollution due to losses of terrestrial carbon pools?, Biogeochemistry, 85(2), 119–123, doi:10.1007/s10533-007-9108-0, 2007.

Obrist, D., Kirk, J. L., Zhang, L., Sunderland, E. M., Jiskra, M. and Selin, N. E.: A review of global environmental mercury processes in response to human and natural perturbations: Changes of emissions, climate, and land use, Ambio, 47(2), 116–140, doi:10.1007/s13280-017-1004-9, 2018.

Park, R. J.: Export efficiency of black carbon aerosol in continental outflow: Global implications, J. Geophys. Res., 110(D11), D11205, doi:10.1029/2004JD005432, 2005.

Perez Catán, S., Bubach, D., Messuti, M. I., Arribére, M. A. and Ribeiro Guevara, S.: Mercury in a geothermal and volcanic area in Patagonia, southern South America, Atmospheric Pollution Research, 11(3), 566–573, doi:10.1016/j.apr.2019.12.005, 2020.

Petzold, A. and Schönlinner, M.: Multi-angle absorption photometry—a new method for the measurement of aerosol light absorption and atmospheric black carbon, Journal of Aerosol Science, 35(4), 421–441, doi:10.1016/j.jaerosci.2003.09.005, 2004.

Phillips, O. L., Lewis, S. L., Baker, T. R., Chao, K.-J. and Higuchi, N.: The changing Amazon forest, Phil. Trans. R. Soc. B, 363(1498), 1819–1827, doi:10.1098/rstb.2007.0033, 2008.

Qiu, R., Han, G., Ma, X., Xu, H., Shi, T. and Zhang, M.: A Comparison of OCO-2 SIF, MODIS GPP, and GOSIF Data from Gross Primary Production (GPP) Estimation and Seasonal Cycles in North America, Remote Sensing, 12(2), 258, doi:10.3390/rs12020258, 2020.

Rose, C., Sellegri, K., Velarde, F., Moreno, I., Ramonet, M., Weinhold, K., Krejci, R., Ginot, P., Andrade, M., Wiedensohler, A. and Laj, P.: Frequent nucleation events at the high altitude station of Chacaltaya (5240 m a.s.l.), Bolivia, Atmospheric Environment, 102, 18–29, doi:10.1016/j.atmosenv.2014.11.015, 2015.

Rose, C., Sellegri, K., Moreno, I., Velarde, F., Ramonet, M., Weinhold, K., Krejci, R., Andrade, M., Wiedensohler, A., Ginot, P. and Laj, P.: CCN production by new particle formation in the free troposphere, Atmos. Chem. Phys., 17(2), 1529–1541, doi:10.5194/acp-17-1529-2017, 2017.

Sanders, A., Verstraeten, W., Kooreman, M., van Leth, T., Beringer, J. and Joiner, J.: Spaceborne Sun-Induced Vegetation Fluorescence Time Series from 2007 to 2015 Evaluated with Australian Flux Tower Measurements, Remote Sensing, 8(11), 895, doi:10.3390/rs8110895, 2016.

Shi, Y., Zhao, A., Matsunaga, T., Yamaguchi, Y., Zang, S., Li, Z., Yu, T. and Gu, X.: High-resolution inventory of mercury emissions from biomass burning in tropical continents during 2001–2017, Science of The Total Environment, 653, 638–648, doi:10.1016/j.scitotenv.2018.10.420, 2019.

Slemr, F., Ebinghaus, R., Brenninkmeijer, C. A. M., Hermann, M., Kock, H. H., Martinsson, B. G., Schuck, T., Sprung, D., van Velthoven, P., Zahn, A. and Ziereis, H.: Gaseous mercury distribution in the upper troposphere

and lower stratosphere observed onboard the CARIBIC passenger aircraft, Atmos. Chem. Phys., 9(6), 1957–1969, doi:10.5194/acp-9-1957-2009, 2009.

Slemr, F., Angot, H., Dommergue, A., Magand, O., Barret, M., Weigelt, A., Ebinghaus, R., Brunke, E.-G., Pfaffhuber, K. A., Edwards, G., Howard, D., Powell, J., Keywood, M. and Wang, F.: Comparison of mercury concentrations measured at several sites in the Southern Hemisphere, Atmos. Chem. Phys., 15(6), 3125–3133, doi:10.5194/acp-15-3125-2015, 2015.

Slemr, F., Weigelt, A., Ebinghaus, R., Kock, H. H., Bödewadt, J., Brenninkmeijer, C. A. M., Rauthe-Schöch, A., Weber, S., Hermann, M., Becker, J., Zahn, A. and Martinsson, B.: Atmospheric mercury measurements onboard the CARIBIC passenger aircraft, Atmos. Meas. Tech., 9(5), 2291–2302, doi:10.5194/amt-9-2291-2016, 2016.

Slemr, F., Martin, L., Labuschagne, C., Mkololo, T., Angot, H., Magand, O., Dommergue, A., Garat, P., Ramonet, M. and Bieser, J.: Atmospheric mercury in the Southern Hemisphere – Part 1: Trend and inter-annual variations in atmospheric mercury at Cape Point, South Africa, in 2007–2017, and on Amsterdam Island in 2012–2017, Atmos. Chem. Phys., 20(13), 7683–7692, doi:10.5194/acp-20-7683-2020, 2020.

Soerensen, A. L., Mason, R. P., Balcom, P. H., Jacob, D. J., Zhang, Y., Kuss, J. and Sunderland, E. M.: Elemental Mercury Concentrations and Fluxes in the Tropical Atmosphere and Ocean, Environ. Sci. Technol., 48(19), 11312–11319, doi:10.1021/es503109p, 2014.

Sprovieri, F., Pirrone, N., Bencardino, M., D'Amore, F., Carbone, F., Cinnirella, S., Mannarino, V., Landis, M., Ebinghaus, R., Weigelt, A., Brunke, E.-G., Labuschagne, C., Martin, L., Munthe, J., Wängberg, I., Artaxo, P., Morais, F., Barbosa, H. de M. J., Brito, J., Cairns, W., Barbante, C., Diéguez, M. del C., Garcia, P. E., Dommergue, A., Angot, H., Magand, O., Skov, H., Horvat, M., Kotnik, J., Read, K. A., Neves, L. M., Gawlik, B. M., Sena, F., Mashyanov, N., Obolkin, V., Wip, D., Feng, X. B., Zhang, H., Fu, X., Ramachandran, R., Cossa, D., Knoery, J., Marusczak, N., Nerentorp, M. and Norstrom, C.: Atmospheric mercury concentrations observed at ground-based monitoring sites globally distributed in the framework of the GMOS network, Atmos. Chem. Phys., 16(18), 11915–11935, doi:10.5194/acp-16-11915-2016, 2016.

Stein, A. F., Draxler, R. R., Rolph, G. D., Stunder, B. J. B., Cohen, M. D. and Ngan, F.: NOAA's HYSPLIT Atmospheric Transport and Dispersion Modeling System, Bull. Amer. Meteor. Soc., 96(12), 2059–2077, doi:10.1175/BAMS-D-14-00110.1, 2015.

Subramanian, R., Kok, G. L., Baumgardner, D., Clarke, A., Shinozuka, Y., Campos, T. L., Heizer, C. G., Stephens, B. B., de Foy, B., Voss, P. B. and Zaveri, R. A.: Black carbon over Mexico: the effect of atmospheric transport on mixing state, mass absorption cross-section, and BC/CO ratios, Atmos. Chem. Phys., 10(1), 219–237, doi:10.5194/acp-10-219-2010, 2010.

Swartzendruber, P. C., Jaffe, D. A. and Finley, B.: Improved fluorescence peak integration in the Tekran 2537 for applications with sub-optimal sample loadings, Atmospheric Environment, 43(22–23), 3648–3651, doi:10.1016/j.atmosenv.2009.02.063, 2009.

Tamburello, G., Hansteen, T. H., Bredemeyer, S., Aiuppa, A. and Tassi, F.: Gas emissions from five volcanoes in northern Chile and implications for the volatiles budget of the Central Volcanic Zone: Volatiles budget of the CVZ, Chile, Geophys. Res. Lett., 41(14), 4961–4969, doi:10.1002/2014GL060653, 2014.

Tassi, F., Aguilera, F., Vaselli, O., Darrah, T. and Medina, E.: Gas discharges from four remote volcanoes in northern Chile (Putana, Olca, Irruputuncu and Alitar): a geochemical survey, Annals of Geophysics, (2), doi:10.4401/ag-5173, 2011.

Venables, W. N. and Ripley, B. D.: Modern Applied Statistics with S, Springer New York, New York, NY., 2002.

Webster, J. P., Kane, T. J., Obrist, D., Ryan, J. N. and Aiken, G. R.: Estimating mercury emissions resulting from wildfire in forests of the Western United States, Science of The Total Environment, 568, 578–586, https://doi.org/10.1016/j.scitotenv.2016.01.166, 2016.

Weisspenzias, P., Jaffe, D., Swartzendruber, P., Hafner, W., Chand, D. and Prestbo, E.: Quantifying Asian and biomass burning sources of mercury using the Hg/CO ratio in pollution plumes observed at the Mount Bachelor observatory, Atmospheric Environment, 41(21), 4366–4379, doi:10.1016/j.atmosenv.2007.01.058, 2007.

Wiedensohler, A., Andrade, M., Weinhold, K., Müller, T., Birmili, W., Velarde, F., Moreno, I., Forno, R., Sanchez, M. F., Laj, P., Ginot, P., Whiteman, D. N., Krejci, R., Sellegri, K. and Reichler, T.: Black carbon emission and transport mechanisms to the free troposphere at the La Paz/El Alto (Bolivia) metropolitan area based on the Day of Census (2012), Atmospheric Environment, 194, 158–169, doi:10.1016/j.atmosenv.2018.09.032, 2018.

Yuan, W., Sommar, J., Lin, C.-J., Wang, X., Li, K., Liu, Y., Zhang, H., Lu, Z., Wu, C. and Feng, X.: Stable Isotope Evidence Shows Re-emission of Elemental Mercury Vapor Occurring after Reductive Loss from Foliage, Environ. Sci. Technol., 53(2), 651–660, doi:10.1021/acs.est.8b04865, 2019.

Zhang, Y., Guanter, L., Berry, J. A., Joiner, J., van der Tol, C., Huete, A., Gitelson, A., Voigt, M. and Köhler, P.: Estimation of vegetation photosynthetic capacity from space-based measurements of chlorophyll fluorescence for terrestrial biosphere models, Glob Change Biol, 20(12), 3727–3742, doi:10.1111/gcb.12664, 2014.

Zhu, C., Kanaya, Y., Yoshikawa-Inoue, H., Irino, T., Seki, O. and Tohjima, Y.: Sources of atmospheric black carbon and related carbonaceous components at Rishiri Island, Japan: The roles of Siberian wildfires and of crop residue burning in China, Environmental Pollution, 247, 55–63, doi:10.1016/j.envpol.2019.01.003, 2019.

Ziskin, D.: Measurements Of Pollution In The Troposphere (MOPITT) Level 3 Gridded Daily CO Retrievals (Thermal Infrared Radiances) (MOP03J) V008, , doi:10.5067/TERRA/MOPITT/MOP03J_L3.008, 2019.